Energy Conversion and Management 283 (2023) 116911

Contents lists available at ScienceDirect

Energy Conversion and Management

journal homepage: www.elsevier.com/locate/enconman

# Optimization of the air loop system in a hydrogen fuel cell for vehicle application

Santiago Martinez-Boggio [a], Davide Di Blasio [b,*], Tom Fletcher [b], Richard Burke [b], Antonio García [a], Javier Monsalve-Serrano [a]

[a] CMT – Motores Térmicos, Universitat Politècnica de València, Camino de Vera s/n, 46022 Valencia, Spain
[b] Department of Mechanical Engineering, University of Bath, Claverton Down, Bath BA2 7AY, UK

ARTICLE INFO

*Keywords:*
Fuel cell
Hydrogen vehicles
Air management
Turbomachinery

ABSTRACT

Hydrogen fuel cells are a potential route to decarbonize the automotive sector due to the zero $CO_2$ tailpipe emissions, faster re-fuelling, and higher energy density than their direct competitor, the battery-electric powertrain. One of the key challenges is to find the best air path configuration to achieve high efficiency in a system level. This work aims to optimize, setup, and demonstrate a highly efficient Proton Exchange Membrane fuel cell system (PEMFC). This powerplant is hydrogen fuelled and scalable to achieve the required power output for different vehicles. This work evaluates a PEMFC by a 1D-numerical approach. The fuel cell is modelled, validated, and later studied under different air inlet conditions. The main goal is the evaluation of different air path layouts to achieve the highest system efficiency. Numerical simulations of electric compressor and coupled and de-coupled electrically assisted turbocharging are performed with different component sizes and cathode pressures. Therefore, this work provides an overview of our initial findings that will outline the key modelling challenges for fuel cell systems and then present a comparison of different air-path architectures. The coupled electrically assisted turbocharger is determined to be the best layout with an improvement of 10% of the delivered power at a high current load. The e-turbocharging optimized by the proposed methodology allows reduction of the peak electric machine electric power by 60%.

## 1. Introduction

Proton exchange membrane fuel cells (PEMFC) are considered a promising propulsion system due to their high efficiency, high power density, and zero tailpipe emission [12]. The fuel cell system consists of four subsystems: fuel cell stack, air supply, hydrogen supply, and water heat management [3]. This technology can be used for stationary applications such as houses [4] and data centers [5] as well as transient conditions as vehicles to produce energy from kilowatts [6] to megawatts [7]. Automotive PEMFC systems operate under pressurized conditions, usually around 2.0–2.5 bar. This improves the fuel cell stack performance, reduces the stack volume and degradation as well as facilitates water management [89]. However, pressurization uses 10–30% of the fuel cell output power [10]. Therefore, the right sizing is crucial for system efficiency, alongside the development of high-efficiency compressors (air inlet), high-efficiency turbines (to recover the energy from the exhaust), and the correct layout architecture [11]. As opposed to internal combustion engines (ICE), the compressor power is higher than the turbine recovery and the use of an external power source, such as an electric machine is mandatory [12]. Compressors, turbines, and electric machines can be coupled in different ways in a charging system. The usage of a numerical model as a matching tool to the right sizing of the air path can save development costs and time [13].

Typical turbocharging design methods depend highly on empirical data and previous experience [14]. As PEMFC is a relatively new type of propulsion system for vehicles, there is a high demand to perform the

*Abbreviations:* PEMFC, Proton Exchange Membrane Fuel Cells; CFD, Computational Fluid Dynamics; DoE, Design of Experiments; EM, Electric Machine; GA, Genetic Algorithm; HD, Heavy Duty; ICE, Internal Combustion Engine; KRPM, Kilo Revolution Per Minute; PID, Proportional Integrative Derivate; PR, Pressure ratio; λ, Air-Fuel Ratio; α, Charge Transfer Coefficient; $C_{fuel\ crossover}$, Open circuit loss due to Fuel Crossover; $\bar{i}_l$, Limiting Current; $R_{ohm}$, Ohm Losses; $a_c$, catalyst-specific area; $L_c$, Catalyst Loading; $E_c$, Activation Energy; $F$, Faraday Constant; $R_{gas}$, Gas Constant; $I$, Current in the Cell; $N_{cells}$, Number of Cells in the Stack; $x$, Mass Fraction; $SR_{cathode}$, Stoichiometric Cathode Ratio; $Eff$, Stack efficiency; $S_i$, Relative Sensitivity.

* Corresponding author.
*E-mail address:* ddb35@bath.ac.uk (D. Di Blasio).

https://doi.org/10.1016/j.enconman.2023.116911
Received 19 December 2022; Received in revised form 13 February 2023; Accepted 6 March 2023

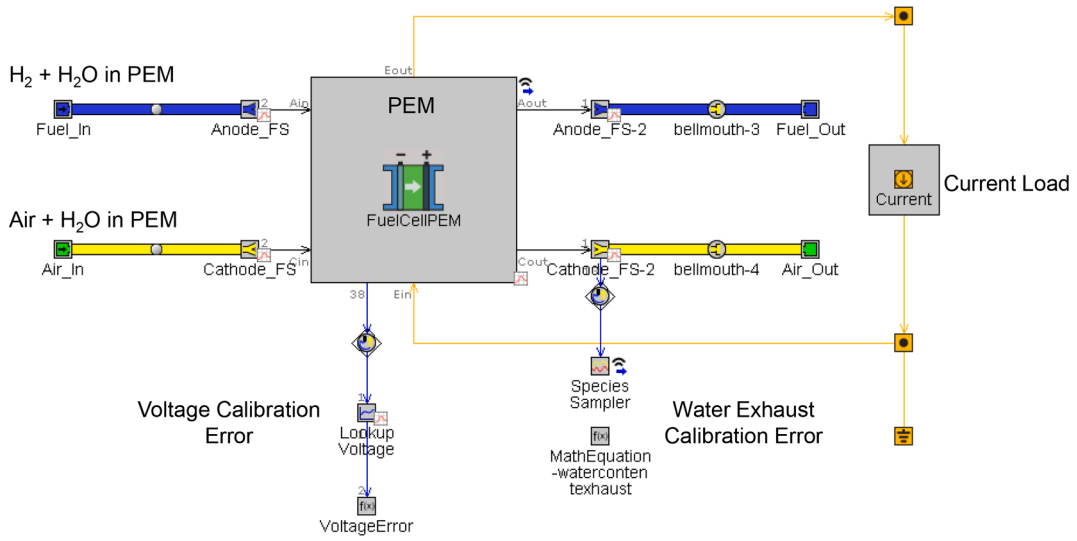


**Fig. 1.** PEMFC basic model with fix input and output conditions used for polarization curve parameter fitting and PEMFC sub-model efficiency study.

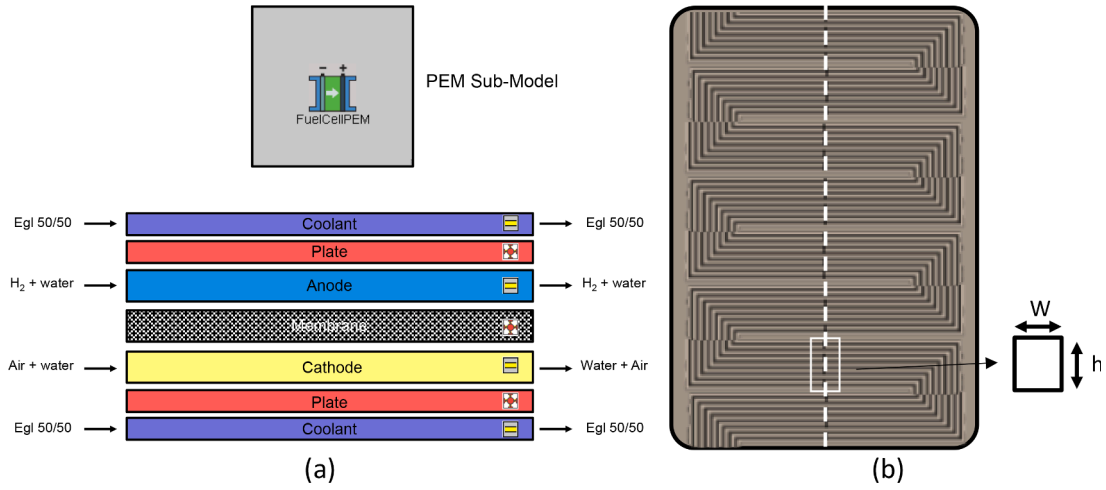


**Fig. 2.** PEMFC sub-model scheme with an explanation of layers modelling (a) and anode/cathode flow channels (b).

**Table 1**
Calibration range for the polarization curve parameters for the PEMFC sub model.

| Parameter | Range Min | Range Max |
|---|---|---|
| **Open Cell Voltage Loss $\Delta V_{oc}$ [V]** | 0.2 | 0.6 |
| **Charge Transfer Coefficient $\alpha$ [-]** | 0.5 | 200 |
| **Exchange Current Density $i_o^{ref}$ [A/m$^2$]** | 15,000 | 30,000 |
| **Limiting Current Density $i_l$ [A/m$^2$]** | 0.03 | 1.0 |
| **Internal Ohmic Resistance $R_{ohm}$ [mOhm]** | 0 | 0.30 |

preliminary design of turbocharging for high pressure and low air flow in the compressor as well as at low temperatures in the turbine. This study aims to address this demand by the evaluation of different air path layouts, compressor, and turbine designs. The PEMFC stack used is representative of powertrain applications and the analysis is performed over a wide range of current requests. The present study shows validation of the stack predictive model in terms of electric power generated and water production at different cathode pressures and temperatures. In addition, the data for modelling the compressor and turbine comes from several experimental results performed in the past. Three different airpath layouts are modelled with three compressor maps and three turbine maps in 18 operating conditions. The main novel aspect of the work is the optimization strategy that allows a comparison between different turbocharger topologies and sizing with the aim to select the best air path in terms of total system efficiency. This is possible due to a virtual hydrogen fuel cell system including gas path (hydrogen, air, and exhaust lines) as well as the stack. Different from previous results that can be found in the bibliography [1516], the proposed work adds the validation of the system with a conventional air path layout (e-compressor), and it is applied a genetic algorithm to choose the best configuration. This allows to find the optimal setup with a low computational cost compared with a design of experiments [17] or detailed 3D CFD models [18]. In addition, it is no-based on an expert decision as it is common to be applied in this type of system [19].

## 2. Literature review

Typically, a PEMFC operates more efficiently with high air inlet pressure and enough airflow to double the oxygen consumed in the reaction ($\lambda \approx 2$) [20]. In addition, for vehicle application fast air response (<1 s) is required for energy management and membrane dry-up prevention [21]. Kerviel et al. [22] identified that centrifugal and roots compressors are the most suitable for fuel cells due to the fact they are smaller and cheaper than screw and scroll compressors. The most common architecture is an electrified centrifugal compressor due to its

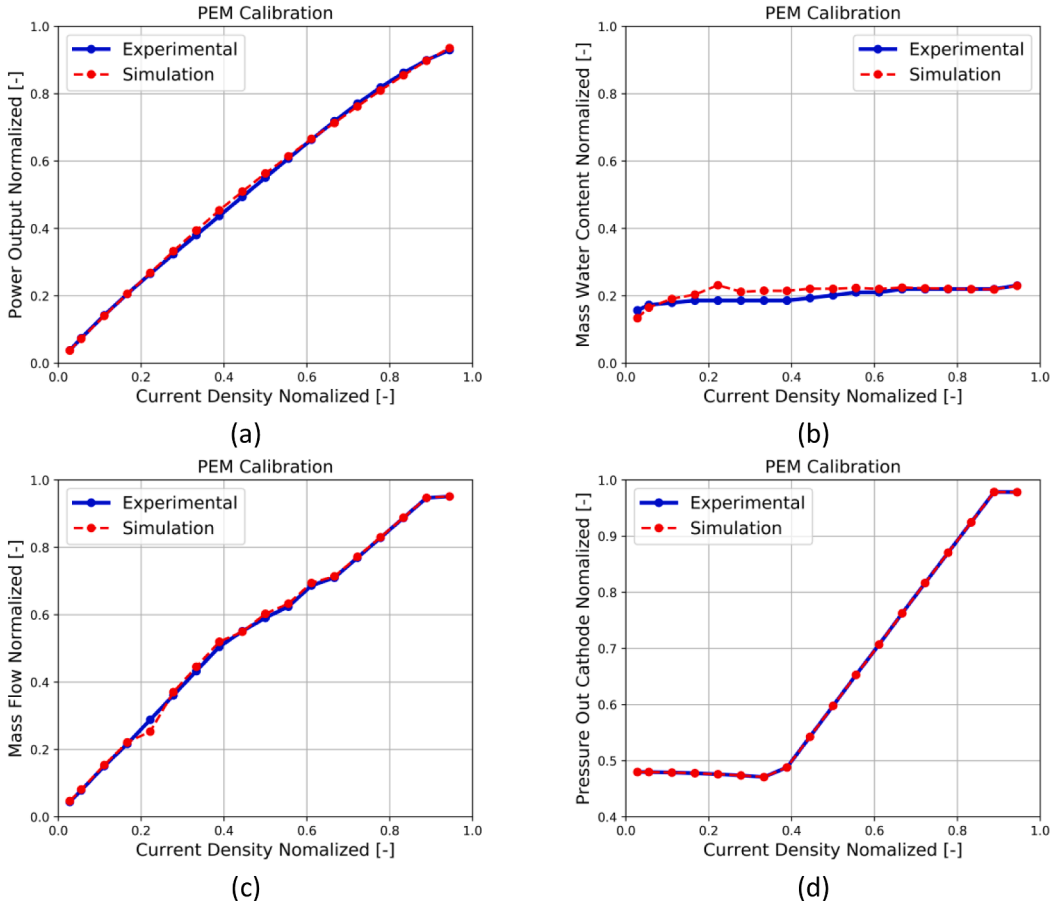


**Fig. 3.** PEMFC calibration in terms of electric power output (a), mass water fraction output (b), air mass flow at the outlet (c), and average cathode pressure (d).

compact size and reduced cost. Few works are focused on the air loop system for high power stacks and none in terms of system layout comparison. The control system is another critical aspect of PEMFC due to the high pressure requirements even at low mass flow [23], the compressor can easily enter in surge region during quick transients [24]. In this area, the air flow rate becomes uncontrollable and can cause damage to the compressor. Toyota [25] developed a strategy to solve the surge avoidance challenge by controlling three inlet air variables: flow rate by electric machine power control, inlet stack pressure by back pressure valve, and bypass rate by a valve that deviates the compressor outlet flow to the exhaust instead of the stack [26]. The development of this strategy was performed by physical modelling of each component and integrated into a system-level simulation. Through vehicle testing, excellent controller air supply performance and surge avoidance in various driving conditions like high temperatures or altitude was confirmed. This shows the potential of numerical modelling to improve air loop transient operation and system efficiency for vehicle PEMFC. Deng et al. [27] presented a novel nonlinear controller design based on cascade adaptive sliding mode control for e-compressor air supply. The results show that the proposed strategy performs better than the conventional constant sliding mode control and PID method in transient operation. Despite several studies showing the performance of electrified compressors in PEMFC operation, the vast majority focus on light-duty vehicles, and few study energy recoveries.

The exhaust energy from the fuel cell stacks can be recovered to the greatest possible extent via the reasonable design and matching of expanders (20–50% of the power consumed by compressors) [28]. The current expanders for PEMFC mainly include screw-type, root-type, scroll-type, and turbine-type. The turbine design is the most promising technology for fuel cells because of the low weight, compact structure, high efficiencies, and the good knowledge of in-vehicle application acquired with ICE vehicles [29]. However, the temperatures of a PEMFC exhaust stream are 80–120 °C, which is much lower than the working fluid temperature of a typical ICE turbine ≈950 °C [30]. Therefore, fuel cells open a new field for new investigations. Zhang et al. [31] studied different turbine configurations by a CFD approach in a 100-kW stack. It was found that a configuration with the turbine plus a wastegate valve could fully recover the exhaust energy at low and medium loads. The turbine plus back pressure valve only shows good performance at high loads. The configuration with the turbine variable nozzle could fully recover the exhaust energy over the whole operating condition range. However, it is shown that can greatly increase the cost and complexity of the supercharging system. The turbine plus back pressure valve is generally preferred because is much less expensive due to the fixed geometry and the simple, passive controls of the back-pressure valve. However, the effect of the coupling with the compressor and electric motor was not studied in this work. Mao et al. [32] performed a CFD study of four non-design structural parameters including blade inlet incline angle, blade thickness, blade tip clearance, and blade number on the aerodynamic performance and internal flow of the rotor. Inlet forward-incline rotor is seen as the best layout for low-temperature turbines as fuel cell stacks. The mass flow rate is increased by 5% when blade thickness is reduced from 1.2 mm to 0.4 mm. However, the study is focused on one single operating condition and system efficiency is not shown. Crespi et al. [33] studied different airpath layouts for the innovative megawatt scale plant for stationary applications. The system operating at mild pressurized conditions (1.7 bar) allows significantly higher net system efficiency, despite the increasing auxiliary consumptions. The additional energy recovery from the cathode exhaust with an expander gives higher net power and net efficiency, adding up to 2% and

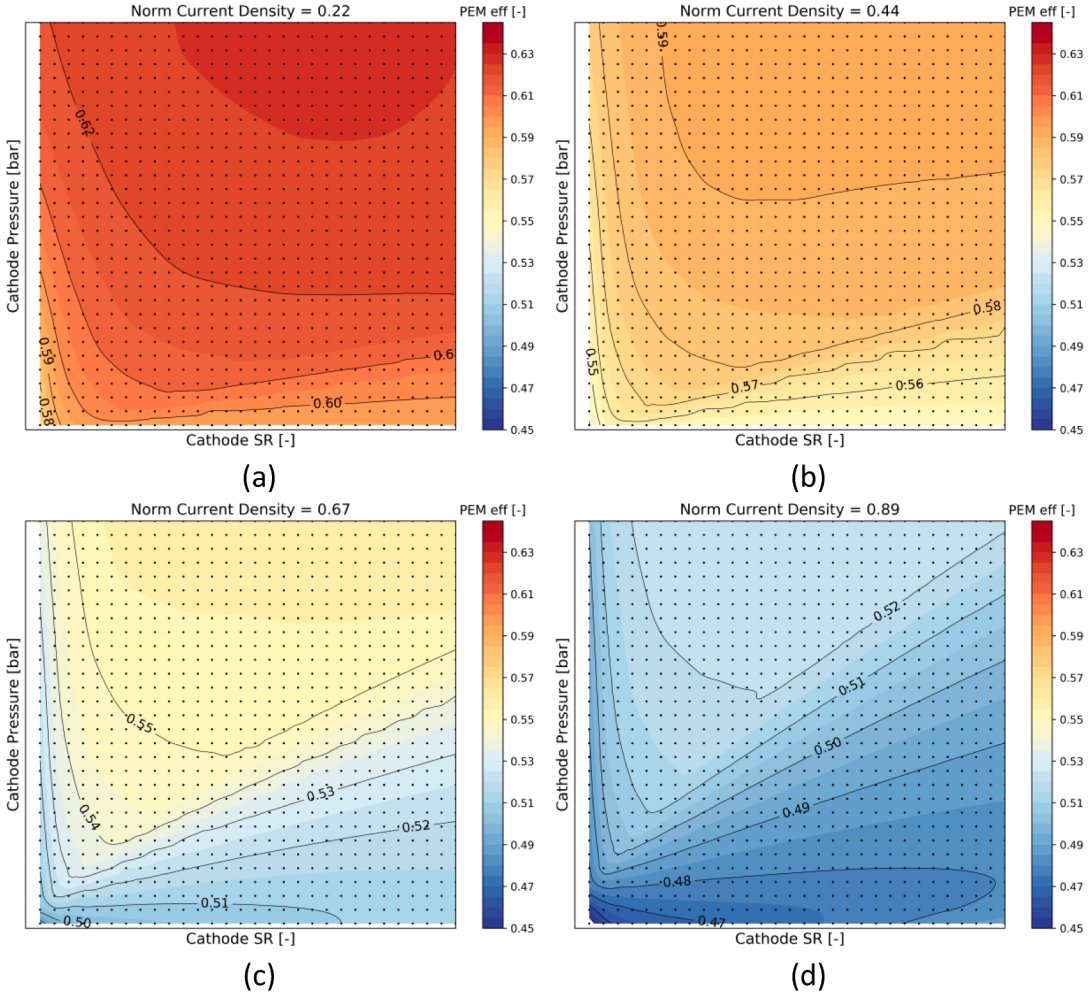


**Fig. 4.** PEMFC efficiency under different cathode air set up (Pressure and Stoichiometric Ratio) for 4 different operative conditions.

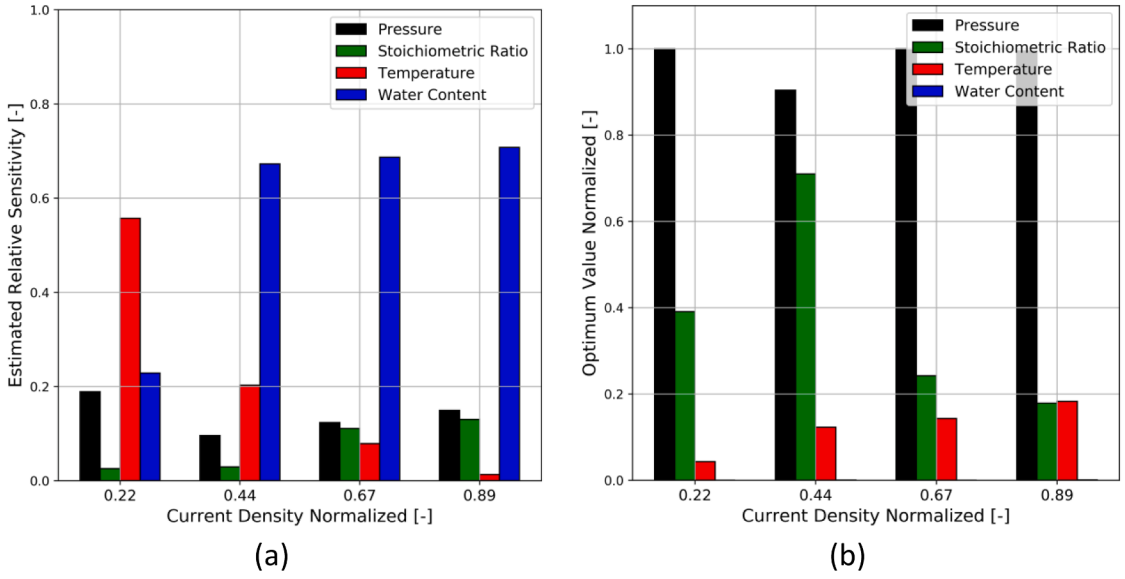


**Fig. 5.** PEMFC relative sensitivity (a) and optimum values normalized to the maximum tested (b) in terms of air inlet conditions: pressure, mass flow, temperature, and water content.

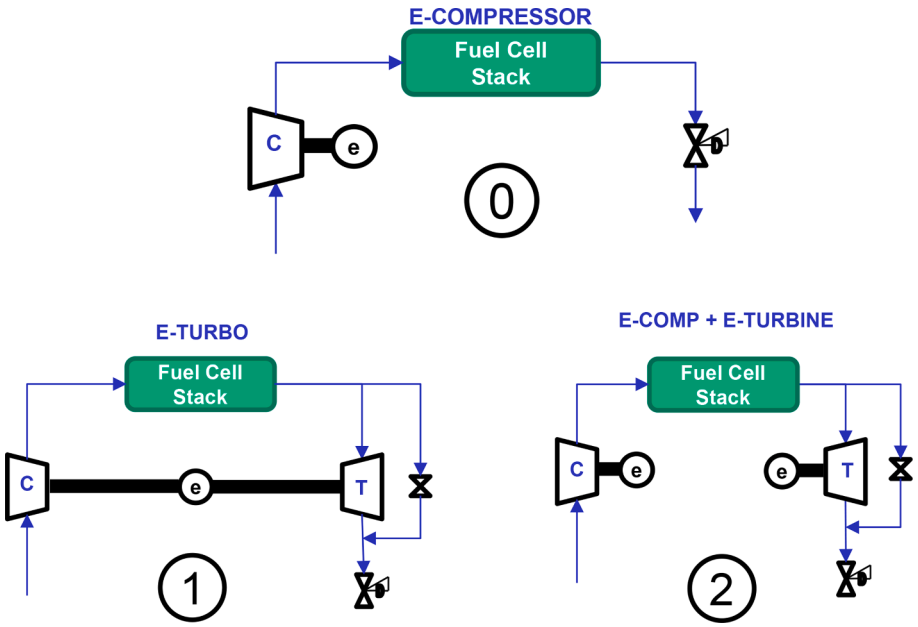


**Fig. 6.** Air loop architectures to be studied.

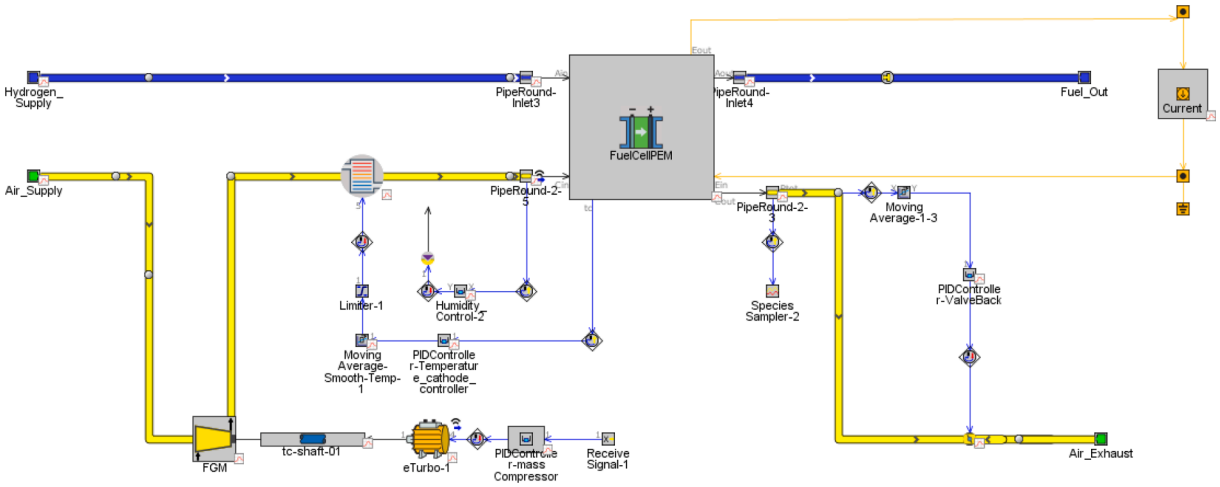


**Fig. 7.** PEMFC complete model for e-compressor configuration (baseline).

reaching system efficiency values between 47% at rated load and 55% at 20% of the rated load.

## 3. Methodology

In the first part of this section the fuel cell numerical model and the validation process against manufacturer data will be presented. In the second part, the baseline electric compressor (e-compressor) air system is shown as well as two proposed electrically assisted turbocharger (e-turbo) configurations. The main target of these new test cases is to improve the overall PEMFC efficiency from a global system perspective.

### 3.1. Fuel cell specifications and numerical model

The fuel cell model is based in a PEMFC designed for vehicle application. Operative conditions have been provided by the fuel cell manufacturer. However, for reason of confidentiality absolute values and details of the experimental set-up cannot be shown. However normalized results will be presented. The focus of this work is to show an optimization methodology for generic fuel cell.

The manufacturer results showed in this work were done in an experimental test bed in which 18 operative conditions were tested. The anode and cathode stoichiometric ratio (ratio between delivered and consumed $H_2$ and $O_2$, respectively) is maintained fixed for all operative conditions to have a comparative point.

The modelling is performed in GT-Suite (v2022, Gamma Technologies®) where the PEMFC sub-model is calibrated using the manufacturer data. Fig. 1 shows the schematic representation of the model. The PEMFC anode and cathode inlet and outlet conditions (mass flow, temperature, and water content) are set as fixed values for each case. This allows precise calibration of the model by replication of the experimental conditions. The current load request is done by an electric connection with a constant signal proportional to the current density.

In the calibration, a genetic algorithm is used with target two parameters. The Non-dominated Sorting Genetic Algorithm III (NSGA-III) [34] is chosen. Because of the exponential increase in the number of non-dominated solutions with the increase in dimensions, most existing domination based evolutionary multi-objective optimization (EMO) algorithms do not scale up to more than three objectives. To alleviate this, new algorithms have been recently proposed mostly using an external

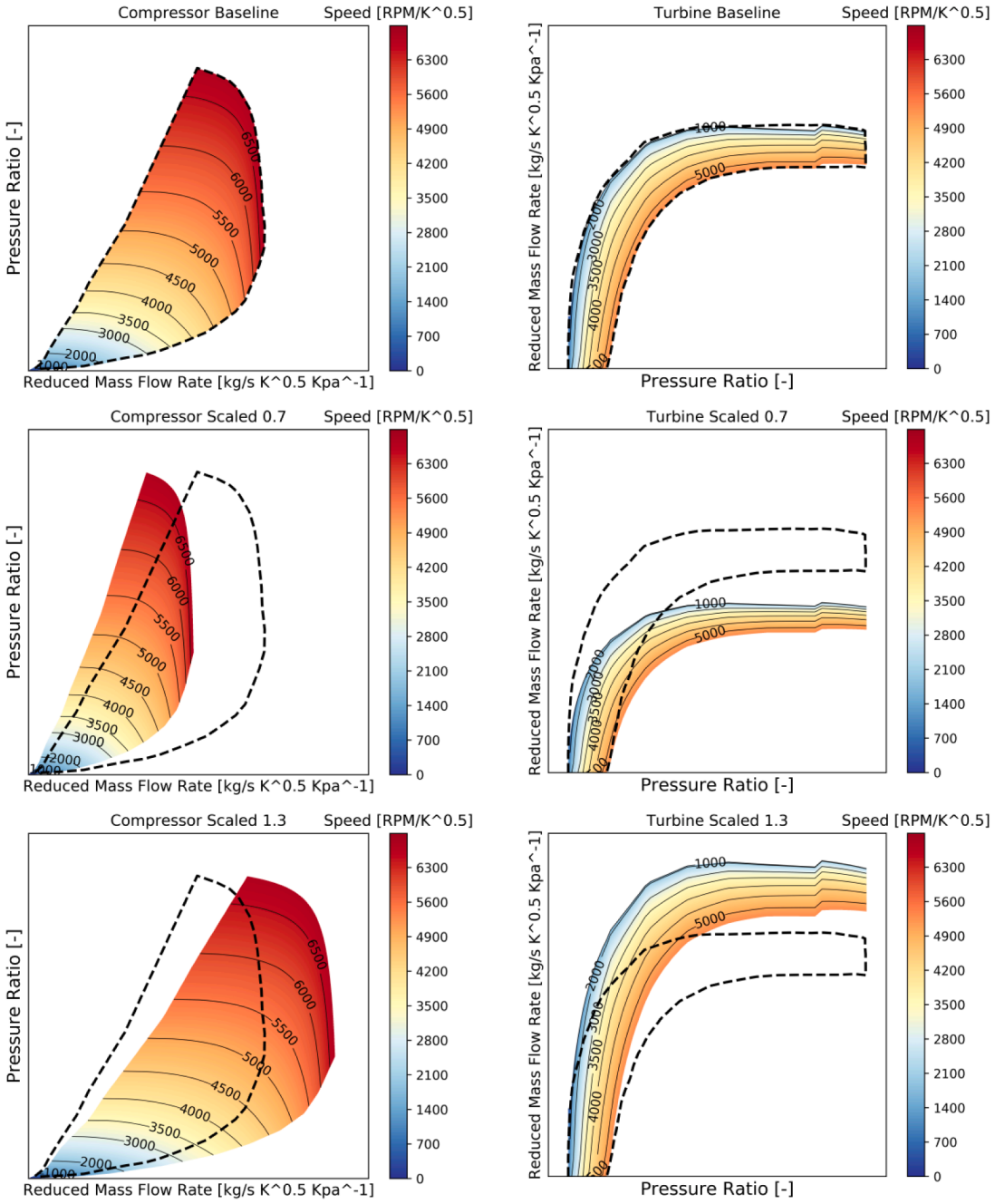


**Fig. 8.** Compressor (left) and Turbine (right) efficiency maps in terms of pressure ratio and reduced mass flow rate for baseline map and scaled maps.

guidance mechanism to help the algorithm distribute its population along a higher-dimensional efficient front. In particular, NSGA-III is based on reference directions which need to be provided when the algorithm is initialized. From the splitting front, some solutions need to be selected. NSGA-III fills up the underrepresented reference direction first. If the reference direction does not have any solution assigned, then the solution with the smallest perpendicular distance in the normalized objective space is surviving. In case a second solution for this reference line is added, it is assigned randomly. Thus, when this algorithm converges, each reference line seeks to find a good representative non-dominated solution. For more information about the genetic algorithm can be found in Seada et al. [35]. This GA is already implemented in GT-Suite, the software used for the numeric analysis.

The voltage (electric power) generated and the water in the cathode exhaust. The first parameter is important to have the same power output between the model and the real PEMFC and the second parameter allows to adjust the water content on the cathode and anode side. This also helps to model the membrane humidity [36]. In the NSGA, seven parameters are calibrated that include five parameters related to the constants on the PEMFC polarization curve model and two parameters that regulate the water molar fraction in anode and cathode inlet.

The PEMFC sub model in GT-SUITE is simulated by layers. The proton conductive membrane in the middle. Anode and Cathode on top of each side of the membrane and last layers of cooling plates and coolant flow channels. Fig. 2a shows a layer representation of the PEMFC sub-model. In 2b the cathode and anode tubes are represented. For this case, the tubes are square with a total length of 240 mm. Although it is possible to model the heat transfer in the PEMFC [37], this work assumes ideal external thermal management. This is acceptable due to much slower dynamics of the fuel cell temperature compared to

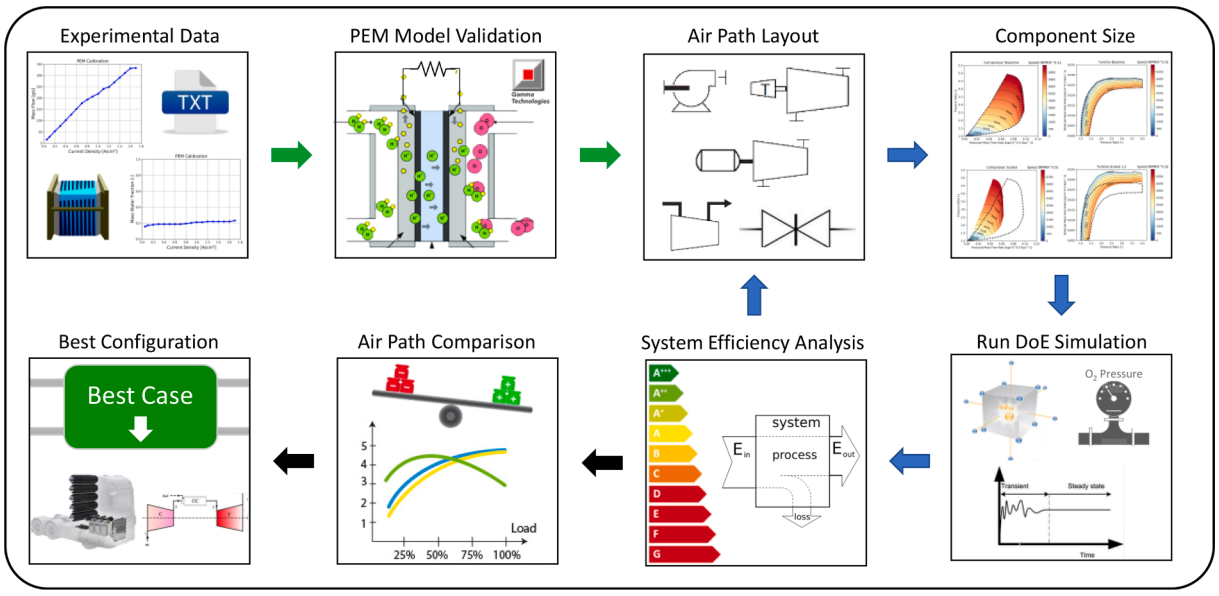


**Fig. 9.** Workflow diagram for air path optimum selection.

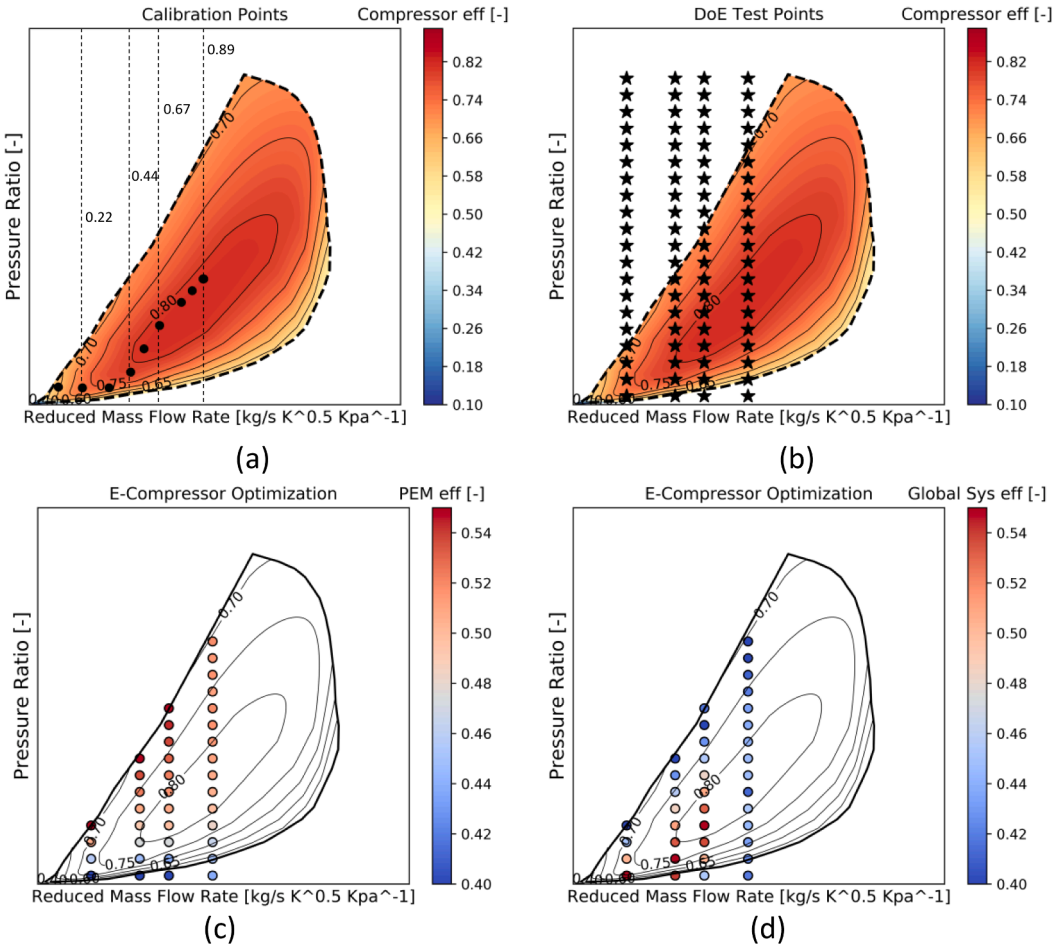


**Fig. 10.** Optimization results for several cathode air pressure under five operative conditions (0.22, 0.44, 0.67 and 0.89 normalized current density). Calibrated experimental points (a), DoE proposal pressure ratio study (b), PEMFC efficiency (c), and PEMFC system efficiency (d) over the compressor baseline map.

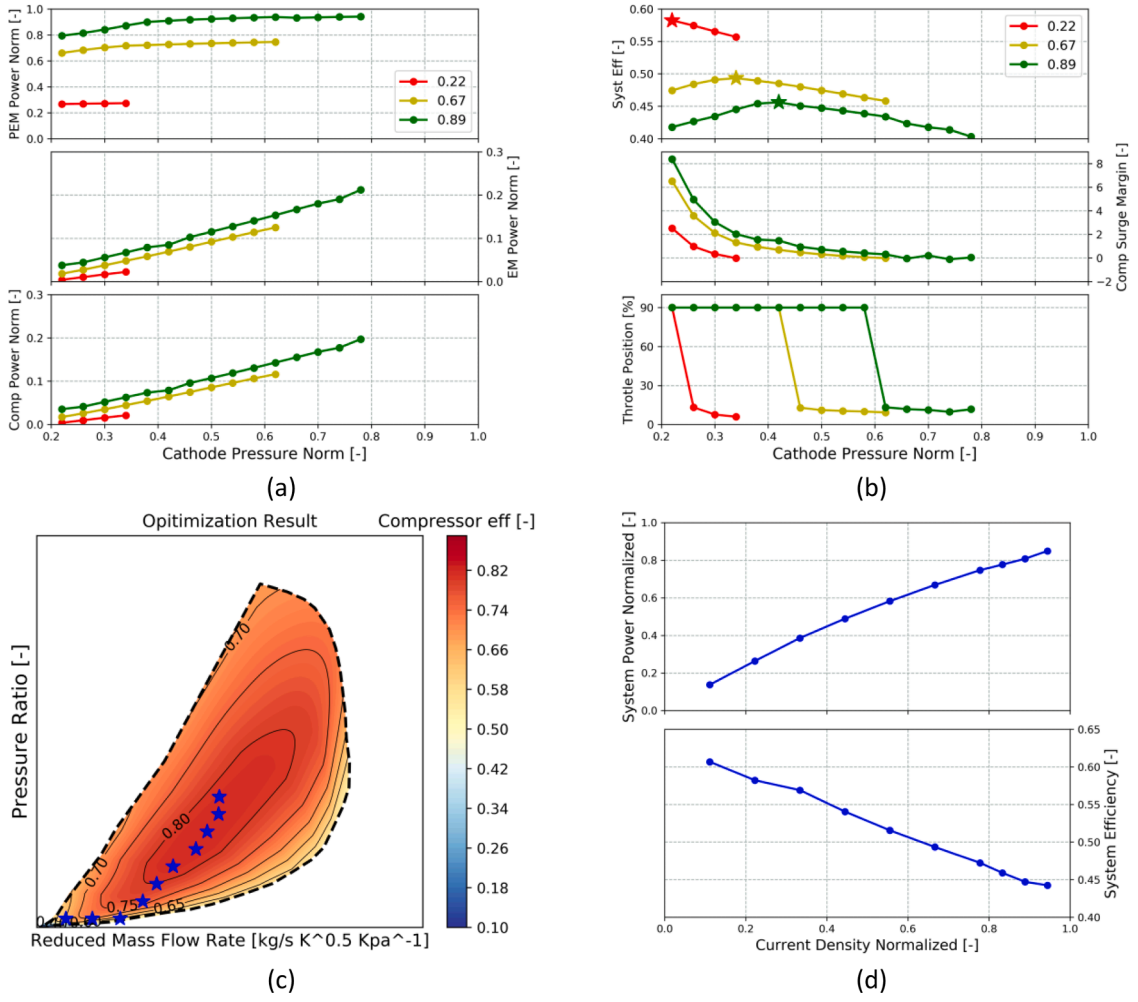


**Fig. 11.** E-compressor PEMFC power, EM power, and compressor power (a) and the system efficiency, compressor surge margin, and throttle position (b) against different cathode pressure. Final optimum points for e-compressor architecture in the compressor efficiency map (c) and final power and system efficiency (d).

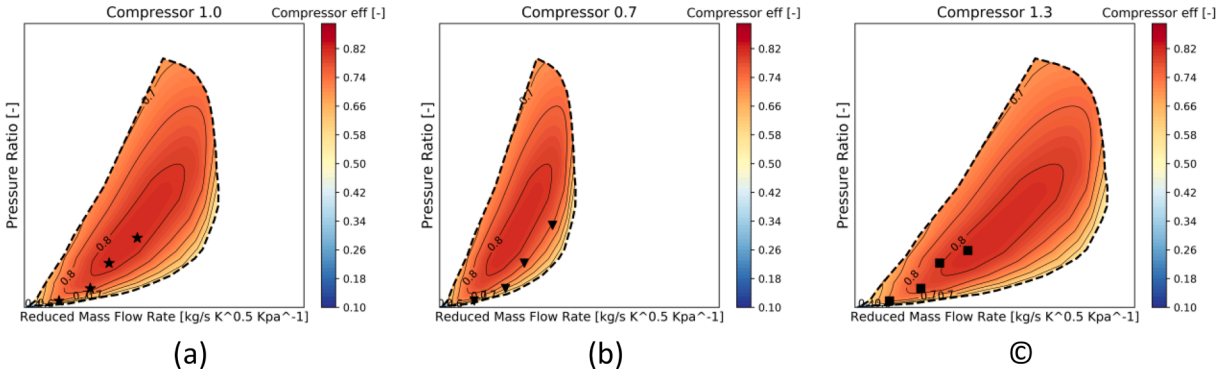


**Fig. 12.** Optimum points for e-compressor architecture at 0.22, 0.44, 0.67, 0.89 normalized current density when using baseline map (a), downsize scaled map (b), and upper size scaled map (c).

those of the reactant flow. The following chemical reactions equation will be used by the software:

$$H_2(g) \rightarrow 2H^+ + 2e^-[anode] \quad (1)$$

$$\frac{1}{2}O_2(g) + 2H^+ + 2e^- \rightarrow H_2O(l)[cathode] \quad (2)$$

$$H_2(g) + \frac{1}{2}O_2(g) \rightarrow H_2O(l)[Overall] \quad (3)$$

where $H_2(g)$ is gaseous hydrogen, $O_2(g)$ is gaseous oxygen, $H^+$ is a positively charged hydrogen ion, $e^-$ is electron, $H_2O(l)$ is liquid water.

Equation (4) is the polarization curve that follows the approach shown by Babir [20]. The fuel cell potential ($V_{cell}$) is equal to the difference between the maximum theoretical potential ($V_{OC}$) of the cell (Equation (5)) minus all the losses ($\Delta V_{oc}, V_{act}, \Delta V_{mt} and \Delta V_{ohm}$) described

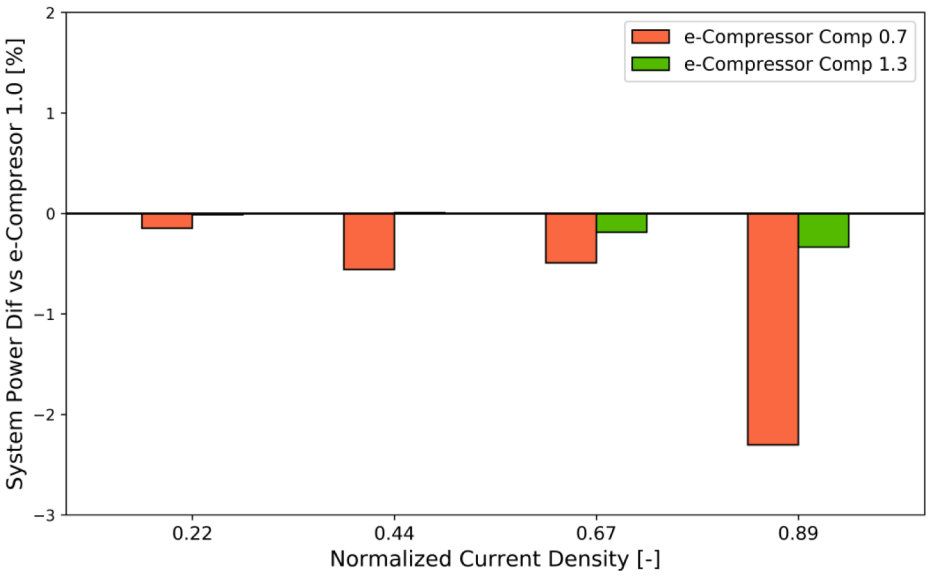


**Fig. 13.** System efficiency gain for scaled maps versus base line map in four current loads.

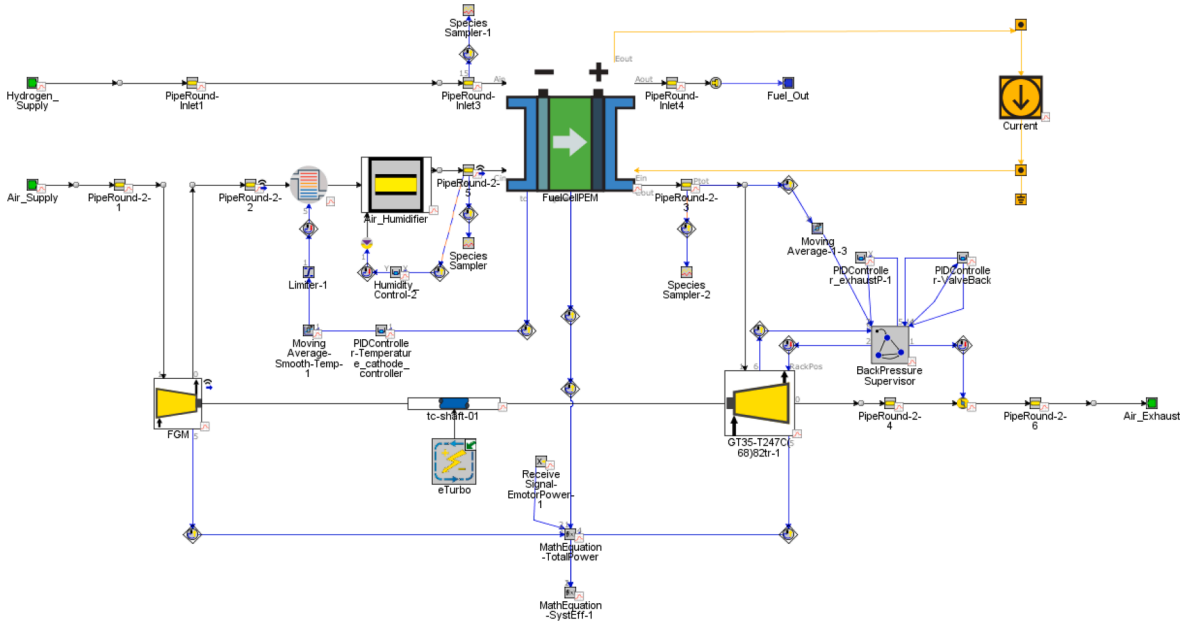


**Fig. 14.** GT-Suite model for the electrified turbocharging with coupled compressor and turbine. The back-pressure supervisory is in charge to control the cathode pressure by the variation of waste gate mass and back pressure valve position.

from Equation (4) to Equation (9).

$$V_{cell} = V_{OC} - \Delta V_{oc} - \Delta V_{act} - \Delta V_{mt} - \Delta V_{ohm} \tag{4}$$

$$V_{oc} = V_o + \frac{R_{gas} \bullet T}{2 \bullet F} \bullet Ln\left(\frac{P_{H_2} \bullet {P_{O_2}}^{0.5}}{P_{H_2O}}\right) \tag{5}$$

$$\Delta V_{oc} = C_{fuelcrossover} \tag{6}$$

$$V_{act} = \frac{R_{gas} \bullet T}{2 \bullet \alpha \bullet F} ln\left(\frac{i}{i_0}\right) \tag{7}$$

$$\Delta V_{mt} = -\frac{RT}{nF} ln\left(1 - \frac{i}{i_l}\right) \tag{8}$$

$$\Delta V_{ohm} = i^* R_{ohm} \tag{9}$$

$$i_0 = {i_0}^{ref} a_c L_c \left(\frac{P_{O_2}}{P_{ref}}\right)^{\gamma} \left[e^{E_c/R}\left(\frac{1}{T_{ref}} - \frac{1}{T_{cell}}\right)\right] \tag{10}$$

The open circuit loss due to fuel crossover $C_{fuel\ crossover}$ [38], the Charge Transfer Coefficient ($\alpha$) [39],the reference exchange current density (${i_o}^{ref}$), the limiting current $i_l$ and the ohim losses $R_{ohm}$ are the five constant parameters that will be calibrated. In addition, $a_c$ is the catalyst-specific area and $L_c$ is the catalyst loading. $P_{ref}$ and $T_{ref}$ are the reference pressure and temperature, respectively. The $E_c$ is the activation energy, $F$ the faraday constant, $R_{gas}$ the gas constant and $\gamma$ pressure dependency coefficient.

To calibrate the other two parameters, the water molar fraction in anode inlet and the water molar fraction in the cathode inlet, dynamic calculation of ohmic resistance based on cell temperature and membrane humidity and crossover of species through the membrane is per-

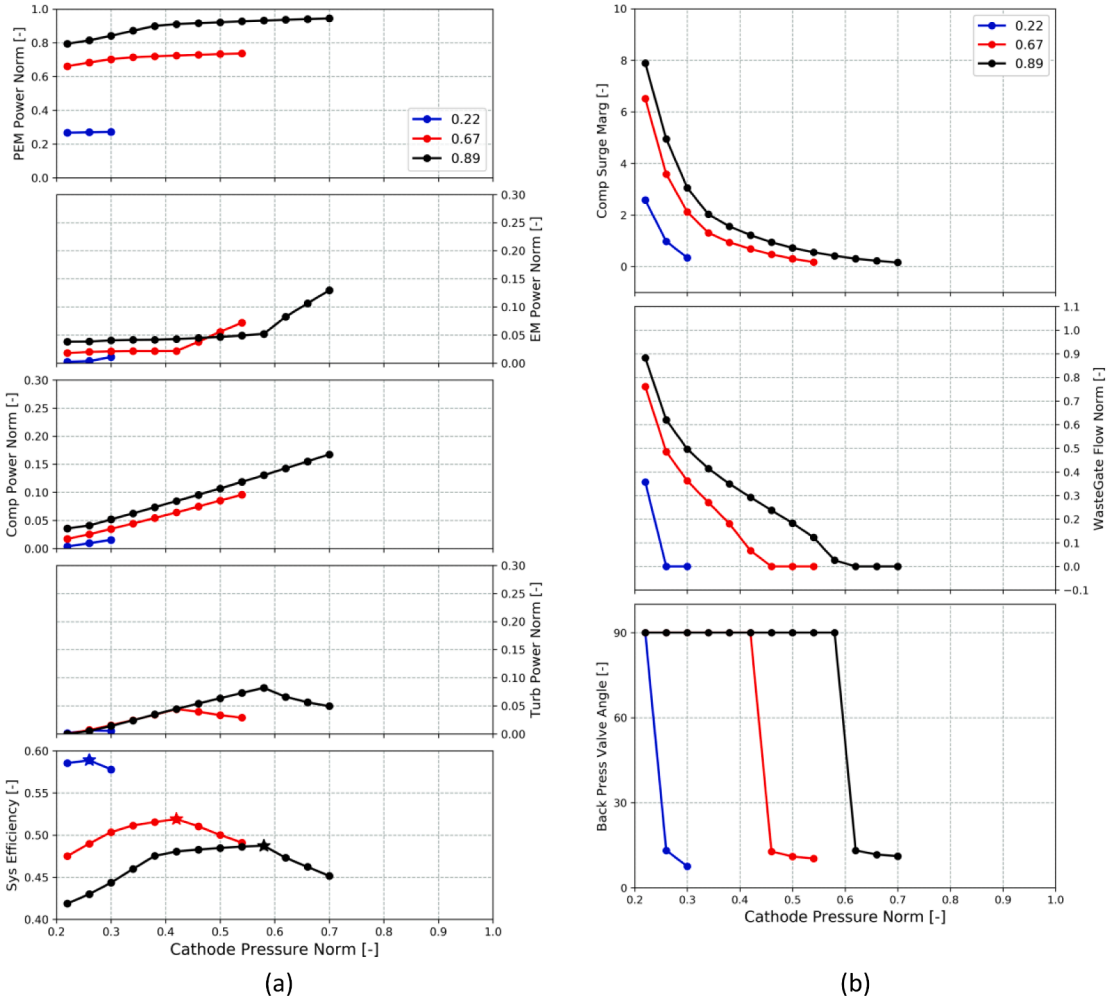


**Fig. 15.** Cathode pressure target influence in component power and system efficiency (a). Other parameters as compressor surge margin, compressor outlet temperature, system speed, waste gate flow, and back pressure valve position against cathode pressure target (b).

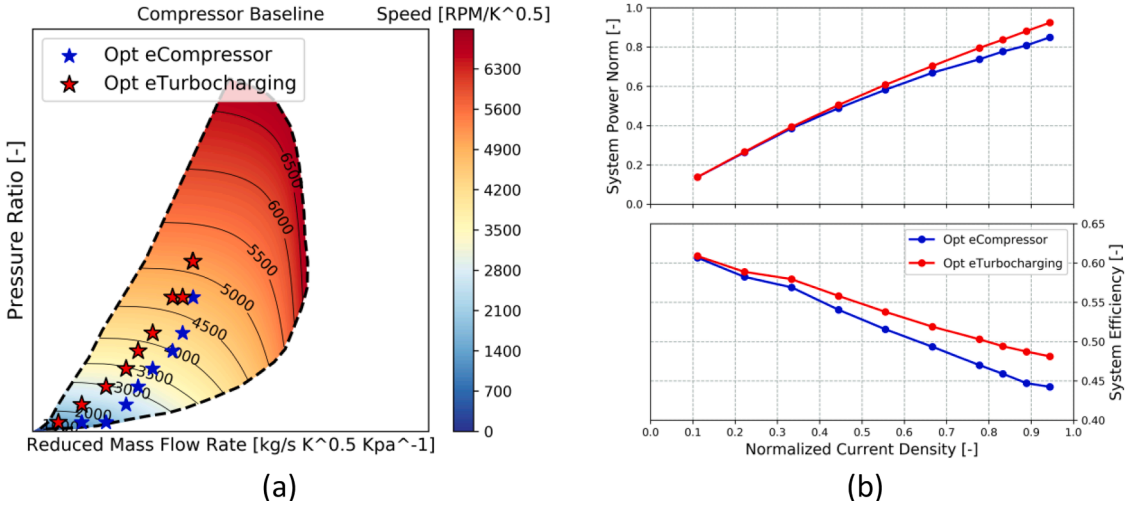


**Fig. 16.** Optimum points for e-turbocharging architecture in the compressor efficiency map (a) and final power and system efficiency (b). E-Compressor optimum is added for comparison.

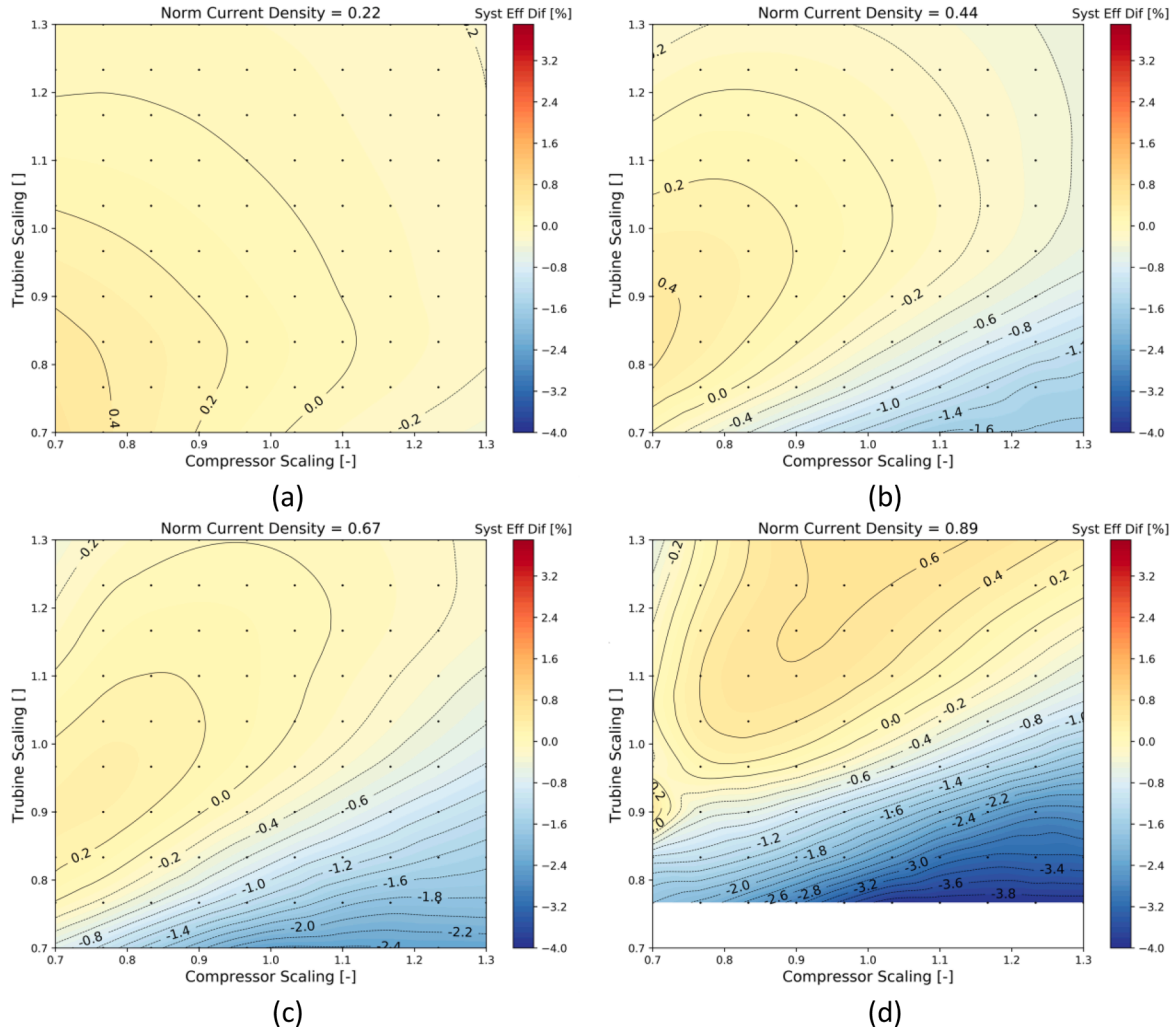


**Fig. 17.** PEMFC system efficiency for the e-turbocharging coupled (case 1) under different map selection using the scaling method. Compressor 1.0 and Turbine 1.0 represent the baseline maps.

formed. The oxygen and hydrogen consumed are calculated using the relationship between the current requested and the number of cells on the stack. From Equation (11) and Equation (12) is possible to see that both quantities are proportional to the current request. The results along this study will compare different configurations at the same current request. This means that the comparison between cases is an equal hydrogen consumption (equal hydrogen mass flow at the inlet of the anode) for all cases. Therefore, the configuration with the maximum electric generation power will be the case with the highest PEMFC efficiency.

$$\dot{m}_{H2,consumed} = \frac{M_{H2}{}^{*}I^{*}N_{cells}}{2^{*}F} \tag{11}$$

$$\dot{m}_{O2,consumed} = \frac{M_{O2}{}^{*}I^{*}N_{cells}}{4^{*}F} \tag{12}$$

$$\dot{m}_{H2,feed} = \frac{\dot{m}_{H2,consumed}{}^{*}\lambda_{anode}}{x_{H2}} \tag{13}$$

$$\dot{m}_{Air,feed} = \frac{\dot{m}_{O2,consumed}{}^{*}\lambda_{air}}{x_{O2}} \tag{14}$$

with $\dot{m}_{H2,consumed}$ the mass flow of hydrogen consumed, $\dot{m}_{O2,consumed}$ the oxygen mass flow consumed. Also, $\dot{m}_{Air,feed}$ and $\dot{m}_{H2,feed}$ the air and hydrogen mass flow that enter the fuel cell, respectively. $M_{H2}$ and $M_{O2}$ the hydrogen and oxygen molecular weight, $I$ the current in the fuel cell, $N_{cells}$ the number of cells in the stack, $\lambda$ the air–fuel ratio, and $x$ the mass fraction.

The pressure drop in the cathode tubes is calculated using a simple orifice model parametrised using empirical data.

$$q = C_D{}^{*}A^{*}\sqrt{2^{*}\rho^{*}\Delta p} \tag{15}$$

$q$ is the volumetric flow rate measured by the nozzle , $C_D$ tubes discharge coefficient, $A$ the area of the throat of the tube, $\rho$ is the fluid density upstream of the entry of the tube, $\Delta p$ is the measured pressure drop across the tubes.One other important parameter is the stoichiometric cathode ratio ($SR_{cathode}$) defined as the amount of introduced air ($\dot{m}_{O_2,feed}$) to the consumed in the PEMFC ($\dot{m}_{O_2,consumed}$). The efficiency ($Eff$) defined as follows the electric power output ($ElectricPower_{output}$) divided the fuel energy.

$$SR_{cathode} = \frac{\dot{m}_{O_2,feed}}{\dot{m}_{O_2,consumed}} \tag{16}$$

$$Eff = \frac{ElectricPower_{output}}{\dot{m}_{H_2,consumed}{}^{*}LHV_{H_2}} \tag{17}$$

with $LHV_{H_2}$ the lower heating value of hydrogen.

A summary of the PEMFC optimization parameters and ranges, output by genetic algorithm with a population size of 30 and generation number of 30 (900 simulation cases) in 18 operative conditions (16200 cases), are presented in Table 1. The coefficients are the same for all

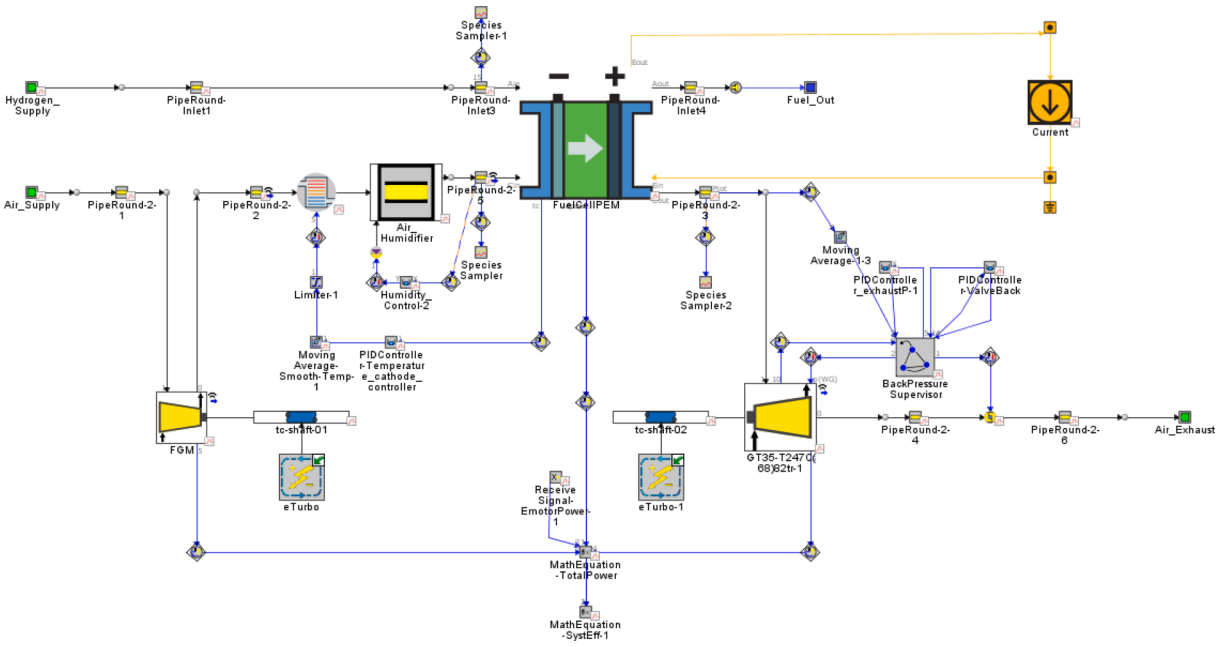


**Fig. 18.** GT-Suite model for the electrified turbocharging with decoupled compressor and turbine. The back-pressure supervisory is in charge to control the cathode pressure by the variation of waste gate mass and back pressure valve position.

current density cases by setting the optimization algorithm in sweep mode instead of on independent. As was mentioned the error for all comparable parameters is $\leq$ 5%. Moreover, the model has a real-time factor equal to 3 and achieves the stationary operation in 0.5 s. Therefore, the complete cases can be obtained in 6.7 h on a conventional desktop computer.

Fig. 3 compares the numerical results to the manufacturer data for the optimization targets, which have been normalized for confidentiality reasons. The optimization method allows calibrating the seven parameters with an average error of 1.1% in power output and 5.0% in cathode water content. These error values are acceptable ($\leq$5%) for a PEMFC model calibrated over 18 current density operation conditions. In addition, Fig. 3 shows the normalized mass flow rate at the cathode output (Air + Water) and the normalized pressure at the outlet. Both parameters have good agreement thanks to the low deviation of the water formation and inlet humidity and the pressure drop calibration in the cathode tubes. With these results is possible to affirm that the PEMFC model is calibrated, and the next steps will be the study in other different inlet conditions to understand the behaviour. The temperature of the PEMFC is imposed during the steady-state simulation with the manufacturer values. The water molar fraction in the anode and cathode were calibrated to adjust the outlet water mass.

### 3.2. Fuel cell optimization study

After the calibration, a full factorial design of experiments was performed in four operative conditions by a 30-level variation of the cathode air flow mass (stoichiometric ratio) and cathode pressure (fuel cell inlet air pressure) while maintaining the other operative parameters equal to the calibration (3600 = 30x30x4). This allows us to understand the potential of different air path layouts in the following sections. Fig. 4 shows the PEMFC efficiency (without including auxiliary power consumption) for stoichiometric ratio ($SR_{cathode}$). Despite a conventional centrifugal compressor typically used in ICE achieving a maximum compression ratio of five, this work extends the range to understand the potential of higher cathode pressures, such as those that can be achieved with double-stage centrifugal compressor or other types of compressors (screw or scroll). In terms of stoichiometric ratio, the literature suggests around $\lambda_{air} = 2.0$ [11]. However, to understand the effect of the air flow in this PEMFC design and size, a much wider range of values has also been examined.

The PEMFC has an increase of efficiency when the cathode pressure increases. This is due to higher exchange current density (Equation (8)) with lower activation losses (Equation (7)). Increasing the airflow mass (increase the stoichiometric ratio) will improve the efficiency of the PEMFC due to a higher presence of $O_2$ even in the latter parts of the cathode channel. The pressure seems to have a higher impact on the efficiency than the SR. However, both parameters contribute to increasing the cell efficiency up to 15% at low and high current densities compare to the minimum value tested.

A genetic algorithm (GA) NSGA-III [40] is used to obtain the best combination of inlet conditions in order to obtain the maximum stack efficiency (no consideration of the system efficiency). This allows to better understand the influence of the inlet air conditions on the PEMFC efficiency. The parameters included in the optimization are:

- Inlet stack pressure.
- Cathode stoichiometric ratio ($SR_{cathode}$).
- System temperature (inlet temperature, stack cooling system temperature, and anode temperature).
- Air molar water content.

The optimum configuration of the GA optimization is the same that the one calculated with the DoE (Fig. 4). However, the results are useful to calculate the relative sensitivity ($S_i$).

$$y_{Efficiency} = a_o + a_1 x_{pressure} + a_2 x_{Stoichiometicratio} + a_3 x_{pressure} + a_4 x_{watermolfraction} \tag{18}$$

$$S_i = \frac{a_i}{\sum |a_i|} \tag{19}$$

where $x_i$ represent standardized factors, $a_i$ represent standardized regression coefficients, and $y_{Efficiency}$ represents the standardized response of the PEMFC efficiency.

Fig. 5 shows the relative sensitivity of the PEMFC efficiency to above parameters. It is shown that the pressure has a higher impact than the stoichiometric ratio with high values preferred as seen in Fig. 4. The temperature and humidity have an important role in the PEMFC output

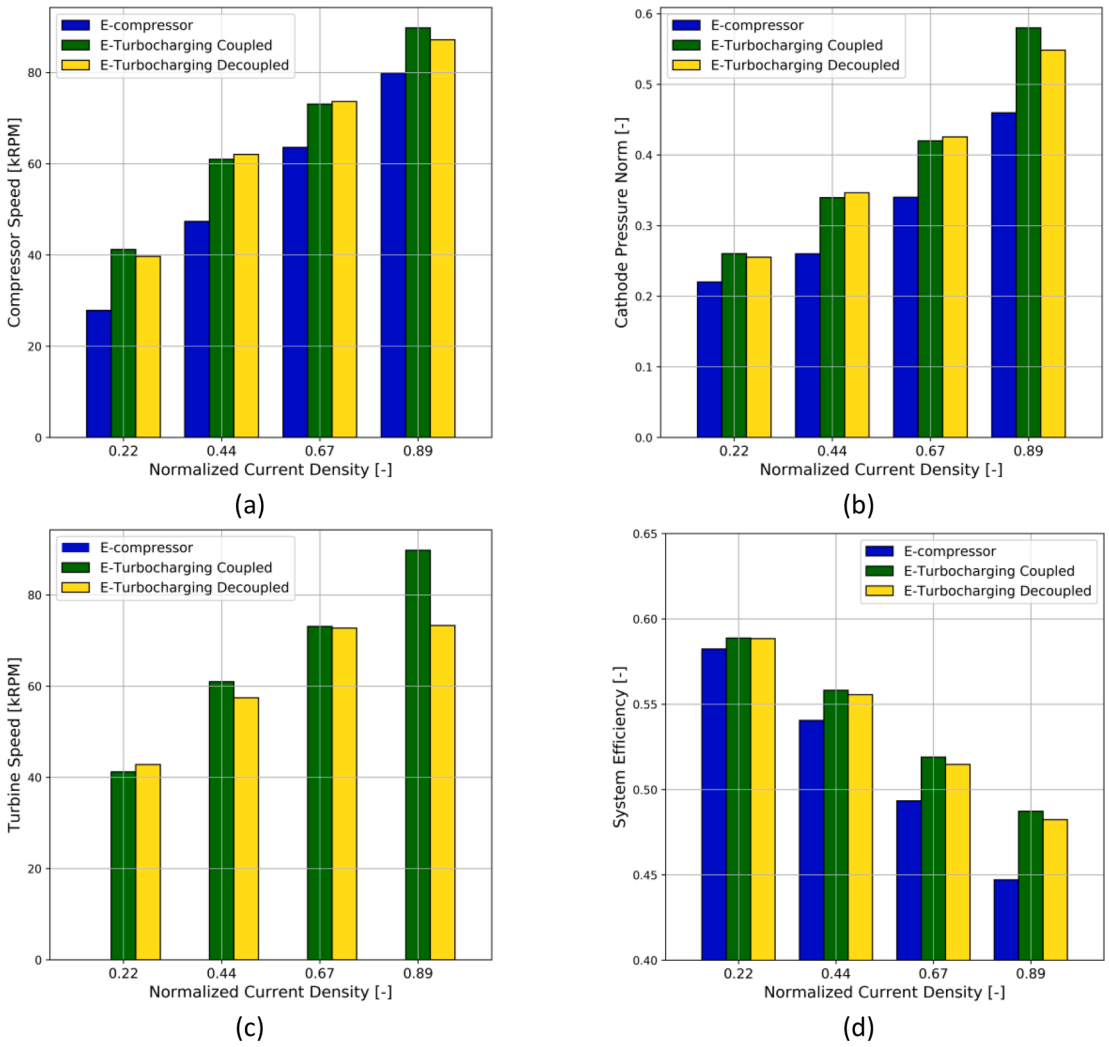


**Fig. 19.** E-turbocharging decoupled compressor speed (a), cathode selected pressure (b), turbine speed (c), and system efficiency (d). E-compressor and E-turbocharging are added for comparison.

power with low values preferred for both components. Fig. 5b depicts the final optimum values normalized by the range tested (1.0 means maximum tested and 0 is the minimum tested). The pressure is always towards the maximum of the range. Meanwhile, the normalised SR is around 0.5 for low load and below 0.3 for high load. The temperature shows optimum towards low-temperature conditions and the cathode humidification water content is zero. The membrane has good operation and performance with the water added only on the anode side.

This analysis has shown that the pressure on the cathode has more influence than the air mass flow and has a more direct impact on system efficiency rather than water content or temperature. These last two factors can be satisfied with a well-designed air conditioner after the compressor (humidifier and heat exchanger) with minimum cost to auxiliary power consumption. However, these ultra-low values of water in the inlet are not suggested due to the degradation of the membrane.

### 3.3. Air loop system model

The focus of this section of work is to use the calibrated PEMFC to evaluate different air path systems to achieve the highest system efficiency by changing the cathode pressure. Three different air path lay-outs (Fig. 6) will be investigated to understand which is the most efficient for Heavy Duty PEMFC.

Case 0 (e-Compressor system, Fig. 7), is a typical air path lay-out used in PEMFC automotive application as the Toyota Mirai. [25]. Case 1 is an e-Turbo system where the compressor and the turbine are coupled by a shaft connected to an electric motor. The rotational speed of all three components is equal. The pressure ratio is controlled by a back-pressure valve after the PEMFC, while the air mass flow is controlled by the power delivered by the electric motor. Case 2 is an e-Compressor plus e-Turbine system which are decoupled. This configuration is more complex due to the additional motor but enables the compressor and turbine speeds to be varied independently. The last two systems allow the energy recovery from the exhaust. Both layouts need a control system capable to manage the backpressure valve and the wastegate valve to control the cathode pressure. The air mass flow is controlled by the power delivered by the Electric Motor (EM).

In all three cases, compressor and turbine components are modelled using a map-based approach. These maps represent a matrix of experimentally measured operative conditions, in terms of speed, pressure ratio, mass flow rate, and thermodynamic efficiency. The electric motor component is also modelled with a map-based approach with two lookup tables that limits the maximum/minimum torque depending on the rotational speed. As shown by Terdich [41] these fast-rotational speed machines have high efficiency in a wide range of torque conditions. A constant EM efficiency of 93% was selected as an average of the cases tested by Terdich [41]. For the calibration process a maximum power of the EM was set at 50 kW to not have mechanical limitation problems. The EM was set to be able to deliver constant torque up to 45 kRPM with the mentioned power capability. At the end of the results

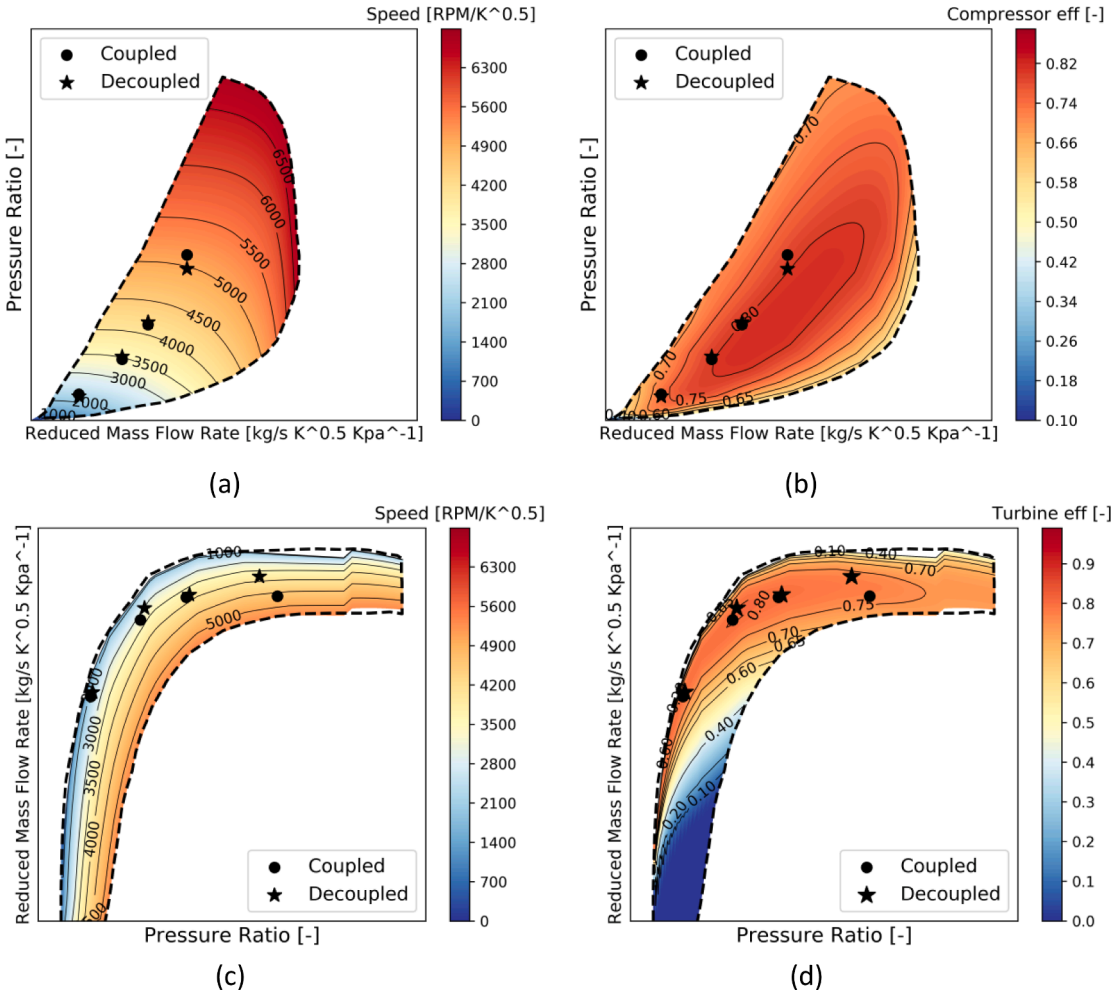


**Fig. 20.** Operative conditions over the baseline compressor speed map (a), compressor efficiency map (b), turbine speed map (c), and turbine efficiency map (d) for the e-compressor decoupled and coupled.

section, a sizing of the electric machine will be performed dependent on the maximum power requirements.

The experimental measurements were performed on a gas stand using the SAE standard [42]. To test several other options, a scaling approach was adopted. Despite, the mass flow multiplier being a simplification, it allows creating a simple scalable model useful for an early system understanding. This approach has been used extensively by several researchers in the bibliography [3143]. Fig. 8 shows a scaling factor of 0.7 and 1.3 for both compressor and turbine. For compressors, the reduction of the mass flow improves the surge line, increasing the possible pressure ratio variation. On the contrary, a scaling factor above 1.0 allows increasing the mass flow with a lower pressure ratio. The optimum selection of the compressor will be a balance between PEMFC efficiency and compressor efficiency matching. In the case of the turbine, the optimum selection will be between the turbine efficiency and the available flow to extract the energy. Therefore, a strong dependence of the operating condition (currently requested by the PEMFC) is expected to be seen.

### 3.4. Case of study

This work proposes a novel methodology where it is possible to select and size the air path layout for a given PEMFC. In this case, the methodology will be applied in vehicle PEMFC following the scheme presented in Fig. 9. The first step is to collect the experimental data for the PEMFC. Eighteen different current density was tested. This data is used in a second step to validate the predictive PEMFC numerical sub-model. The third step is part of a loop where different air path layouts are tested. Several compressor and turbine maps are tested. For each configuration, wastegate turbine flow and back pressure valve position are calibrated to achieve the target cathode pressure. The experimental data for compressor and turbine is needed before starting this step. This was obtained with already test performed for compressor and turbine used for internal combustion engine operation.

Later, a DoE of 20 target cathode pressure in 10 operative conditions (current requested values) are run for each airpath configuration. The ten operative conditions are selected from the eighteen experimental current requests to reduce the simulation time. The PEMFC system efficiency ($System_{Efficiency}$) is analysed by considering all power input and output of the system.

$$System_{Efficiency} = \frac{PEMFC_{electricalpower} - EM_{electricalpower}}{FuelPower} \tag{20}$$

with $PEMFC_{electricalpower}$ the electrical power generated in the PEMFC, $EM_{electricalpower}$ the used electrical power to move the compressor and $FuelPower$ the energy feed in hydrogen to the fuel cell.

Lastly, after running the loop for several air path layouts and maps, the results are compared, and the advantage and drawbacks of each case are analysed. Lastly, the best air path layout is selected. The results in the next section will show, for each architecture layout, the system efficiency when only the operative cathode pressure is optimized and when both pressure cathode and component map are optimized.

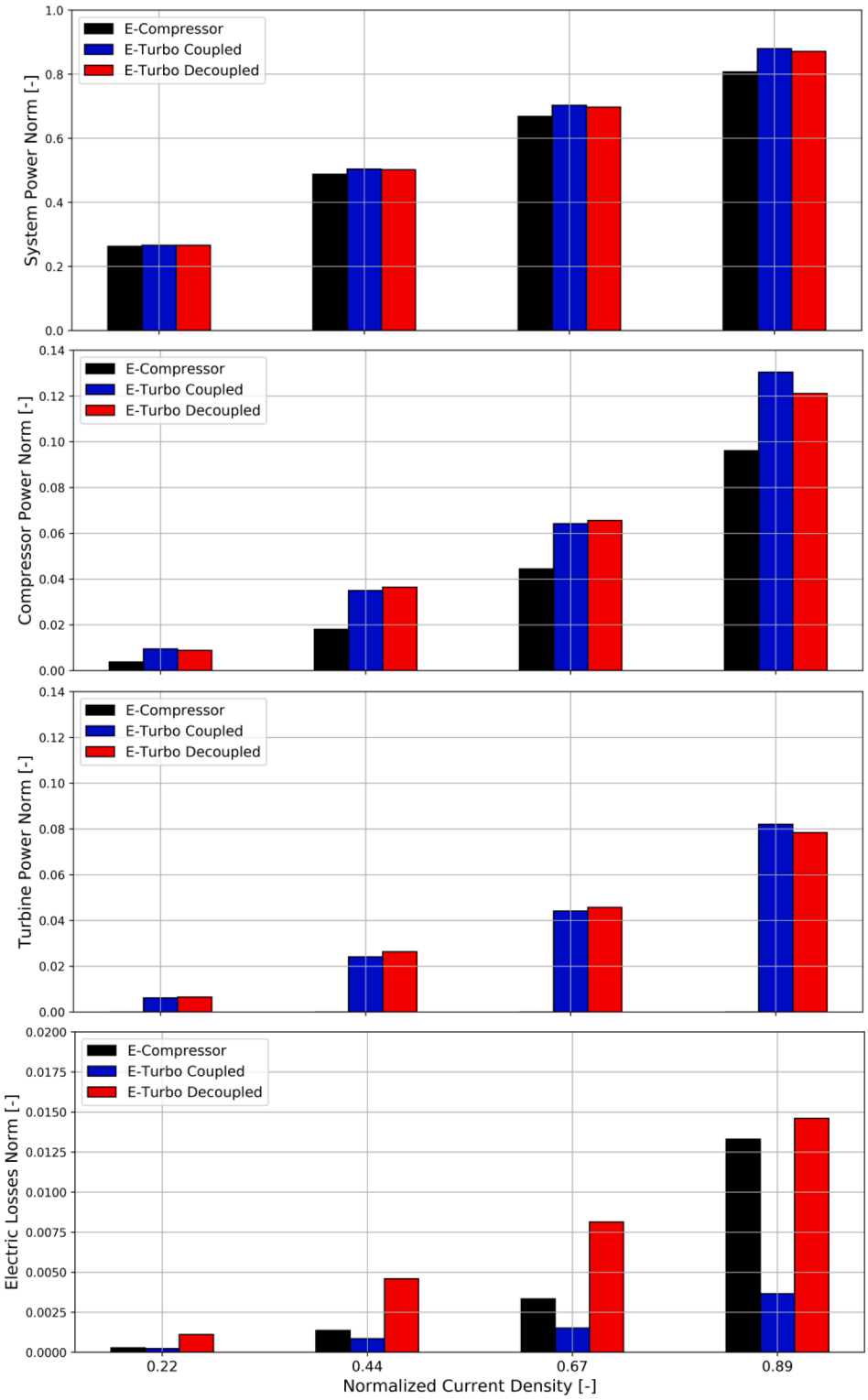


**Fig. 21.** Comparison between the three different air loop types for four current density points in terms of electric machine losses, turbine recovered power, compressor power and total system power.

## 4. Results

The results are divided into a first section with the optimization of the e-Compressor and a second section that shows the optimization for the e-Turbo and e-Compressor plus e-Turbine models.

### *4.1. E-Compressor performance*

The e-Compressor optimisation is performed by a DoE of twenty cathode pressures for ten operative conditions (normalized current density of 0.11, 0.22, 0.33, 0.44, 0.56, 0.67, 0.78, 0.83, 0.89, and 0.94). Fig. 10a shows the calibration points over the baseline compressor map. The calibration points represent the operating conditions of an air path

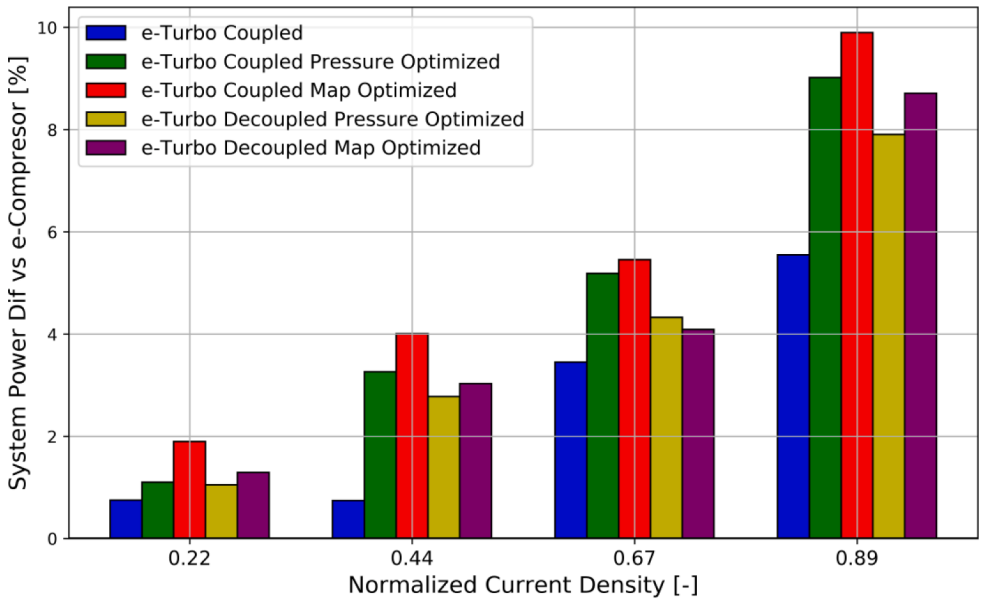


(a)

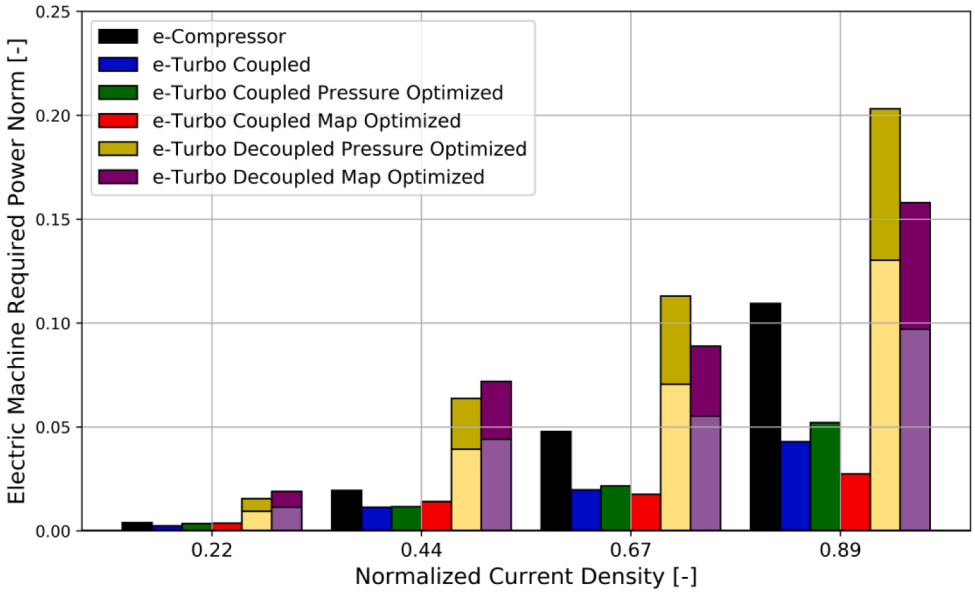


(b)

**Fig. 22.** (a) System power difference between all the air path architectures with different optimization against baseline e-compressor case at four different current request conditions. (b) Electric machine requested electric power for all air path studied at four different current request conditions.

layout that was optimized with traditional tools. All the results presented in the following section are performed with the algorithm shown in Fig. 9.

Fig. 10b shows the proposed 20 new cathode pressure cases over the baseline compressor map for 0.22, 0.44, 0.67, and 0.89 normalized current density. The results in terms of PEMFC efficiency and system efficiency can be seen in Fig. 10c and Fig. 10d, respectively. It is possible to observe that the PEMFC efficiency increases with the pressure, but the system efficiency has an optimum at a medium pressure level. This can be explained by the fact that more compressor power is required when the increasing of pressure ratio. As none of the excess energy in the exhaust is recovered (configuration without turbine), the optimal pressure ratio (cathode pressure) is $<$ 50% of the maximum pressure achievable for this compressor.

The trend in terms of components generating power and consuming power (compressor, e-Motor) is shown in Fig. 11a. It is a proportional relationship between the compressor power and the pressure ratio due to the fixed air mass flow rate. Therefore, the optimum operative condition (cathode pressure) is in the point that the increase of electric consumption is not compensated for more PEMFC generating power. Fig. 11b shows the PEMFC system efficiency behaviour against the pressure cathode where the optimum value is marked with a star.

The optimum operative condition for the compressor is shown in Fig. 11c over the compressor baseline map. In addition, Fig. 11d shows the overall system efficiency for the baseline case in all current density conditions. At low loads, the system efficiency can achieve 60% while at

full load decays until 45%. It is important to note that over the full range of operation this e-Compressor case is more efficient than a diesel engine (up to 42%). The results in this section will be used for comparison with the other air path layouts.

To understand the possible advantage of other compressor sizes, the scaled method presented in the methodology is used. Fig. 12 shows the optimum pressure ratio for four current density loads. In spite that the best compressor efficiency is at a high-pressure ratio for the compressor scaled 0.7, the optimum point is still selected at a low-pressure ratio due to the large amount of energy that needs to be provided and the low gains in terms of PEMFC electrical power generated. Due to a non-optimal map operation, the overall system efficiency for the down-sized scale is worse than the baseline map (see Fig. 13).

### 4.2. Analysis of air loop systems

After testing the baseline case, the other two air path layouts will be investigated. In the first step, the electrified turbocharged with coupled compressor and turbine is evaluated by the model presented in Fig. 14. The cathode pressure is controlled by a back pressure supervisory controller that actuates in the back-pressure valve if the pressure is below the target (wastegate valve fully closed) or by opening the wastegate when the pressure is above the target (back pressure valve fully open). With this controller is possible to vary in steps the cathode pressure. The compressor and turbine have the same speed, and a controller in the electric machine regulates the torque delivered to the shaft to achieve the desired airflow mass. The model is evaluated in the 10 current density operative conditions, but detailed results are presented for 0.22, 0.44, 0.67, and 0.89 normalized current density for the brevity of the manuscript. These four conditions represent low, medium, and high current request load. Therefore, the reader can have an extended overview of the PEMFC behaviour.

Fig. 15 shows the power delivered (PEMFC, turbine) or consumed (compressor, e-Motor) for each one of the components as well as the system efficiency at steady state against the cathode pressure. The optimum case is marked with a star as before. It is possible to observe a linear increase of the compressor power with the increase of cathode pressure. For the turbine, the recovery energy increases until the point where the waste gate is closed, and the back-pressure valve is fully open. After this point, the energy recovered decreased due to a decrease in the pressure ratio in the turbine. Fig. 15 also shows that by increasing the cathode pressure, the compressor operating point moves closer to the surge margin. Maximum cathode pressure allowed is when the surge margin is zero. For all cases the optimum is a point where the compressor operates close to the surge margin, the wastegate is closed and the back-pressure valve is open. This is a remarkable result because allows further investigation for the setting of the waste gate valve and back pressure valve in a fixed position. This reduces the number of calculations and demonstrates that despite the increase of pressure in the cathode for increasing PEMFC efficiency the global efficiency decays.

To understand the differences between the baseline and the new calculations, Fig. 16a shows the operative conditions in the compressor map. The new air path layout works at a higher-pressure ratio due to the possibility of recovering part of the energy in the expander (turbine work). Fig. 16b depicts the system delivered power and efficiency for 10 current density operative conditions. The differences are noticeable at high current density because of more energy to recover in the exhaust. At full load, the e-turbocharging enables the fuel cell to produce 10.3% more electric power. At medium load, the improvements for the e-turbocharging are 5% and at low load 2% with respect to the e-compressor case. The improvement in fuel cell output power is attributed to the lower 'cost' of the compression as a result of the recuperation of energy from the exhaust flow, enabling higher pressures in the stack.

After the study with the baseline compressor and turbine maps, the next step is the evaluation of different turbo-matching. This means testing different compressor and turbine maps. To make the study parametric with the baseline maps, a scaling method is used. As was demonstrated in the previous graph, the optimum condition is when the wastegate is closed and the back-pressure valve is fully open. Fig. 17 shows the system efficiency for four current density conditions with 100 map combinations (full factorial of 10 compressor and 10 turbine levels between 0.7 and 1.3 scaling factor). The results show that the map selection has a higher influence on the system efficiency at high current densities. The maximum improvement is 0.7% in efficiency when the turbine is scaling by 1.3 with the baseline compressor (scaling 1.0) at full load. At low load, the improvement by reducing the compressor and turbine can allow an improvement of 0.4%. For intermediate cases, the benefits are almost negligible. On the other hand, using a smaller turbine for a current density above 0.22 normalized current density can imply system efficiency losses of up to 3%. The worst-case scenario is 0.89 normalized current density because cannot operate below turbine scaling 0.8 due to excessive cathode pressure that leads to the compressor enter in the surge region. Overall, the results show that the baseline compressor map with the turbine scaled 1.3 is the option for this PEMFC system. In addition, the results suggest that turbo-matching is less sensitive for a PEMFC than an ICE where the wrong selection can imply large efficiency losses.

The last air path architecture tested is the decoupled e-Compressor and e-Turbine. This implies an extra electric motor and a degree of freedom. Fig. 18 shows the model scheme with the two-electric motors for driving the compressor and turbine. The control system of the motors is set by a PID controller where the compressor e-Motor delivers the required torque to achieve the desired air mass flow and the turbine e-Motor absorbs the power to set the desired rotational speed. The cathode pressure is controlled as in the previous case by the wastegate and back pressure valve. Like the behaviour of the previous case, the best efficiency was achieved by closing the wastegate and fully opening the back-pressure valve. In addition, the turbine speed optimum case after a full factorial DoE of 120 cases (20 levels of cathode pressure and 6 rotational speed levels) per current load was found close to the optimum turbine efficiency point.

For brevity of the manuscript, the comparison of the best case for the e-turbocharging decoupled and the previously shown cases are depicted in Fig. 19 using the baseline maps. The compressor speed depends on the selected cathode pressure due to the same air flow mass. This can be seen by comparison of Fig. 19a and Fig. 19b. The increase of pressure ratio for the e-turbocharging coupled with the e-compressor was explained in the previous results due to higher PEMFC efficiency and the possibility of recovering the energy of the exhaust. However, for the decoupled case is seen a small decrease in compressor speed is due to the set of lower cathode pressure. This can be explained by a higher cost of the compressor energy because of the decoupling from the turbine and associated losses with energy conversion in the e-Motors. Turbine speed (Fig. 19c) changes for the decoupled case to adjust to the best turbine map region in terms of efficiency. The global efficiency in Fig. 19d decreases for the decoupled case with respect to the coupled air path layout. Despite an improvement in the turbine efficiency, there is a high-efficiency cost to pass the turbine power to the compressor electrically using two electric machines.

The compressor and turbine operation for the optimized cases at 0.22, 0.44, 0.67, and 0.89 normalized current density can be seen in Fig. 20. The lower pressure ratio in the compressor is seen in Fig. 20a, with both operating close to the maximum efficiency in Fig. 20b. On the other hand, Fig. 20c and Fig. 20d show the change in turbine speed to operate at higher efficiency compared to the coupled case that needs to maintain the compressor operation speed.

A power comparison is shown in Fig. 21 to understand the difference between the decoupled case and the previously shown air path layouts. For low and medium current requests there is a benefit in turbine power recovered for the decoupled version due to high-efficiency turbine operating point by controlling turbine speed independently of the

compressor. However, the electric losses are higher for the decoupled case due to the passage of the energy from the turbine to the compressor by two electric motors instead of directly by a mechanical shaft. Therefore, the system efficiency is worse for the decoupled case than the coupled e-turbocharger. Despite this decrease of energy output for the decoupled e-turbocharging, there are still benefits with respect to the e-Compressor configuration due to the turbine's recovered energy. It is important to note that the decoupled version needs to reduce the cathode working pressure at maximum load to reduce the electrical losses on the compressor side. This explains the lower energy recovered in the turbine for the decoupled against the coupled system.

Summarizing, Fig. 22a shows the system efficiency of all air path layouts tested against the baseline (e-Compressor). The e-Turbo Coupled means the compressor and turbine are linked with the same inlet pressure as the e-Compressor. The "Pressure Optimized" results refer to the nominal compressor and turbine maps where the operating pressure only has been optimised. The "Map Optimized" results refer to those where both the operating pressure and map scaling have been optimised.

Overall, the addition of a turbine allows increasing the system efficiency (delivered electric power) between 1% at low load to 8% at full load compared to the e-compressor baseline case. The maximum benefit was achieved with the coupled e-Turbocharging while with an optimized map and the cathode pressure. The gain found is 10% more energy delivered at 0.89 normalized current density. Moreover, the results show an average gain of 3% for applying the cathode pressure optimization strategy to the e-turbocharging coupled configuration. In addition, the map optimization approach allows an extra 1%. Lastly, the decoupling of the shaft shows an average gain of 4.3% compared to the e-Compressor. However, this is 1.0% lower than the e-turbocharging coupled.

The electric required power from the electric machine is depicted in Fig. 22b and could be used for sizing the e-Motor. For the decoupling e-turbocharging case, a double bar colour represents the electric machine to drive the compressor (lower light colour bar) and the electric machine to absorb power from the turbine (upper dark colour bar). The total value shown in Fig. 22b represents the sum of the total power required. As two electric machines, one as motor and the other as a generator, the total power must be large above the other cases. This means a clear disadvantage of the concept. The coupled e-turbocharging allows to drastically reduce the size of the electric machine by 50% from e-compressor to e-Turbo coupled map optimized if the optimization process is applied. This is one extra advantage of the proposed air path layout. It is important to note that the speed requirements were shown in Fig. 19.

## 5. Conclusion

A novel methodology is presented and applied to a PEMFC vehicle applications to design the cathode air path. The fuel cell model was developed and validated with experimental data with an error of 1.1% in PEMFC efficiency and 5.0% in water molar fraction at the outlet. A study of different air stoichiometric ratios and cathode pressures was performed before the optimization of the air path in a 1D PEMFC predictive model to understand the impact of the air conditions. The parameter with more impact on the efficiency is the cathode pressure.

A DoE for several air path layouts and turbomachinery maps was proposed varying the air inlet pressure. In terms of air path layout, the results showed:

- The turbocharging layout with an electric machine assistant in coupled version is the best layout with an improvement of 10% of the delivered power at the highest current load tested (0.89 normalized current density).
- The e-turbocharging optimized by the proposed methodology allows reducing the electric machine requested electric power by 60%. The maximum speed of the EM increases from 80 KRPM to 90 KRPM due to the increase of the cathode pressure.
- The cathode pressure optimization by a DoE allows improving the system efficiency of the e-turbocharging 3.5% at full load and on average 2.0%.
- The map optimization allows an extra 1% of system efficiency increase and reduces the EM size. The optimum map was found for the baseline compressor size and the scaling 1.3 turbine.
- The decoupling of the compressor and turbine allows improving the turbine efficiency. However, the electric losses increase reducing the overall system efficiency. In addition, two bigger electric machines need to be used compared with the e-turbocharging and e-compressor.

Overall, the methodology proposed allows to find the best layout and the right size of the component with a low computational time. For the proposed PEMFC size, the e-compressor coupled directly with a turbine is the best layout at all current requested. The required electric machine is almost half in size as the stock e-compressor version and the power output can almost doubled.

The results found can help to design of more efficient PEMFC at a system level by the right sizing of the components. Future work will be concentrated on transient simulation with the proposed methodology to understand the effect when the current load changes.

### *CRediT authorship contribution statement*

**Santiago Martinez-Boggio:** Conceptualization, Methodology, Software, Validation, Writing – original draft. **Davide Di Blasio:** Data curation, Writing – original draft, Methodology, Investigation. **Tom Fletcher:** Visualization, Investigation, Writing – review & editing. **Richard Burke:** Supervision, Project administration, Funding acquisition. **Antonio García:** Supervision. **Javier Monsalve-Serrano:** Writing – review & editing.

### Declaration of Competing Interest

The authors declare that they have no known competing financial interests or personal relationships that could have appeared to influence the work reported in this paper.

### Data availability

The authors do not have permission to share data.

### Acknowledgments

Santiago Martinez-Boggio would like to thank the UPV for the program: Ayudas para la movilidad dentro de estancias de doctorado de la Universitat Politècnica de València (convocatoria vicerrectorado de investigación, innovación y transferencia 2021).

### References

[1] Liu F, Mauzerall DL, Zhao F, Hao H. Deployment of fuel cell vehicles in China: Greenhouse gas emission reductions from converting the heavy-duty truck fleet from diesel and natural gas to hydrogen. Int J Hydrogen Energy 2021;46(34):17982–97. https://doi.org/10.1016/j.ijhydene.2021.02.198.

[2] Kast J, Vijayagopal R, Gangloff JJ, Marcinkoski J. Clean commercial transportation: Medium and heavy duty fuel cell electric trucks. Int J Hydrogen Energy 2017;42(7):4508–17. https://doi.org/10.1016/j.ijhydene.2016.12.129.

[3] Gößling S, Nickig N, Bahr M. 2-D + 1-D PEM fuel cell model for fuel cell system simulations. Int J Hydrogen Energy 2021;46(70):34874–82. https://doi.org/10.1016/j.ijhydene.2021.08.044.

[4] Cai S, Li X, Li S, Luo X, Tu Z. Flexible load regulation method for a residential energy supply system based on proton exchange membrane fuel cell. Energy Convers Manag 2021;258(December):2022. https://doi.org/10.1016/j.enconman.2022.115527.

[5] Zhao J, Chang H, Luo X, Tu Z, Chan SH. Dynamic analysis of a CCHP system based on fuel cells integrated with methanol-reforming and dehumidification for data centers. Appl Energy 2022;309(December 2021):118496. https://doi.org/10.1016/j.apenergy.2021.118496.

[6] Zhao J, Cai S, Luo X, Tu Z. Multi-stack coupled energy management strategy of a PEMFC based-CCHP system applied to data centers. Int J Hydrogen Energy 2022;47(37):16597–609. https://doi.org/10.1016/j.ijhydene.2022.03.159.

[7] Fan L, Tu Z, Chan SH. Technological and Engineering design of a megawatt proton exchange membrane fuel cell system. Energy 2022;257:124728. https://doi.org/10.1016/j.energy.2022.124728.

[8] Dhimish M, Vieira RG, Badran G. Investigating the stability and degradation of hydrogen PEM fuel cell. Int J Hydrogen Energy 2021;46(74):37017–28. https://doi.org/10.1016/j.ijhydene.2021.08.183.

[9] Xiao B, Zhao J, Fan L, Liu Y, Chan SH, Tu Z. Effects of moisture dehumidification on the performance and degradation of a proton exchange membrane fuel cell. Energy 2022;245:123298. https://doi.org/10.1016/j.energy.2022.123298.

[10] Carcadea E, et al. Effects of geometrical dimensions of flow channels of a large-active-area PEM fuel cell: A CFD study. Int J Hydrogen Energy 2021;46(25):13572–82. https://doi.org/10.1016/j.ijhydene.2020.08.150.

[11] Hoeflinger J, Hofmann P. Air mass flow and pressure optimisation of a PEM fuel cell range extender system. Int J Hydrogen Energy 2020;45(53):29246–58. https://doi.org/10.1016/j.ijhydene.2020.07.176.

[12] Di Ilio G, Di Giorgio P, Tribioli L, Bella G, Jannelli E. Preliminary design of a fuel cell/battery hybrid powertrain for a heavy-duty yard truck for port logistics. Energy Convers Manag 2021;243:114423. https://doi.org/10.1016/j.enconman.2021.114423.

[13] Arif M, Cheung SCP, Andrews J. A systematic approach for matching simulated and experimental polarization curves for a PEM fuel cell. Int J Hydrogen Energy 2019;45(3):2206–23. https://doi.org/10.1016/j.ijhydene.2019.11.057.

[14] Yu X, Chang H, Luo X, Tu Z. Experimental study on the dynamic performance of an air-cooled proton exchange membrane fuel cell stack with ultra-thin metal bipolar plate. Int J Hydrogen Energy 2022;no. xxxx. https://doi.org/10.1016/j.ijhydene.2022.08.177.

[15] Xia Q, Zhang T, Sun Z, Gao Y. Design and optimization of thermal strategy to improve the thermal management of proton exchange membrane fuel cells. Appl Therm Eng 2023;222(August 2022):119880. https://doi.org/10.1016/j.applthermaleng.2022.119880.

[16] Kampker A, Heimes H, Kehrer M, Hagedorn S, Reims P, Kaul O. Fuel cell system production cost modeling and analysis. Energy Rep 2023;9:248–55. https://doi.org/10.1016/j.egyr.2022.10.364.

[17] Zhao J, Li X, Shum C, McPhee J. Control-oriented computational fuel cell dynamics modeling – Model order reduction vs. computational speed. Energy 2023;266(August 2022):126488. https://doi.org/10.1016/j.energy.2022.126488.

[18] Zhang Y, He S, Jiang X, Xiong M, Ye Y, Yang X. Three-dimensional multi-phase simulation of proton exchange membrane fuel cell performance considering constriction straight channel. Energy 2023;267(November 2022):126544. https://doi.org/10.1016/j.energy.2022.126544.

[19] Hamdollahi S, Jun L. a Review on Modeling of Proton Exchange Membrane Fuel Cell. Chem Ind Chem Eng Q 2023;29(1):61–74. https://doi.org/10.2298/CICEQ220126014H.

[20] Kim B, Cha D, Kim Y. The effects of air stoichiometry and air excess ratio on the transient response of a PEMFC under load change conditions. Appl Energy 2015;138:143–9. https://doi.org/10.1016/j.apenergy.2014.10.046.

[21] Macauley N, Watson M, Lauritzen M, Knights S, Wang GG, Kjeang E. Empirical membrane lifetime model for heavy duty fuel cell systems. J Power Sources 2016;336:240–50. https://doi.org/10.1016/j.jpowsour.2016.10.068.

[22] Kerviel A, Pesyridis A, Mohammed A, Chalet D. An evaluation of turbocharging and supercharging options for high-efficiency Fuel Cell Electric Vehicles. Appl Sci 2018;8(12):pp. https://doi.org/10.3390/app8122474.

[23] Liu Z, et al. Real time power management strategy for fuel cell hybrid electric bus based on Lyapunov stability theorem. Int J Hydrogen Energy 2022;no. xxxx. https://doi.org/10.1016/j.ijhydene.2022.08.176.

[24] Desantes JM, Novella R, Pla B, Lopez-Juarez M. Impact of fuel cell range extender powertrain design on greenhouse gases and NOX emissions in automotive applications. Appl Energy 2021;302. https://doi.org/10.1016/j.apenergy.2021.117526.

[25] Tomi N, Hasegawa S, Farnsworth J, Imanishi H, Ikogi Y, Sato K. Development of Air Supply Controller for FCV Based on Model-Based Development Approach. SAE Tech Pap 2021;2021:1–12. https://doi.org/10.4271/2021-01-0742.

[26] Luca R, Whiteley M, Neville T, Shearing PR, Brett DJL. Comparative study of energy management systems for a hybrid fuel cell electric vehicle - A novel mutative fuzzy logic controller to prolong fuel cell lifetime. Int J Hydrogen Energy 2022;47(57):24042–58. https://doi.org/10.1016/j.ijhydene.2022.05.192.

[27] Deng H, Li Q, Cui Y, Zhu Y, Chen W. Nonlinear controller design based on cascade adaptive sliding mode control for PEM fuel cell air supply systems. Int J Hydrogen Energy 2019;44(35):19357–69. https://doi.org/10.1016/j.ijhydene.2018.10.180.

[28] Zhang Y, Xu S, Lin C. Performance improvement of fuel cell systems based on turbine design and supercharging system matching. Appl Therm Eng Nov. 2020;180. https://doi.org/10.1016/j.applthermaleng.2020.115806.

[29] Fischer T, Willers OW, Seume JR. Preliminary design of a partial admission turbine for waste heat recovery in fuel cells. Inst Mech Eng 2018:3–16. - 13th Int. Conf. Turbochargers Turbocharging 2018.

[30] García A, Monsalve-serrano J, Martinez-boggio S, Gaillard P. Emissions reduction by using e-components in 48 V mild hybrid trucks under dual-mode dual-fuel combustion. Appl Energy 2021;vol. 299, no. May:117305. https://doi.org/10.1016/j.apenergy.2021.117305.

[31] Zhang Y, Xu S, Lin C. Performance improvement of fuel cell systems based on turbine design and supercharging system matching. Appl Therm Eng 2020;vol. 180, no. July:115806. https://doi.org/10.1016/j.applthermaleng.2020.115806.

[32] Mao H, Zhang Y, Xu S. Design and Structural Parameters Analysis of the Turbine Rotor in Fuel Cell Vehicle. SAE Tech Pap 2021;2021:1–7. https://doi.org/10.4271/2021-01-0729.

[33] Crespi E, Guandalini G, Gößling S, Campanari S. Modelling and optimization of a flexible hydrogen-fueled pressurized PEMFC power plant for grid balancing purposes. Int J Hydrogen Energy 2021;46(24):13190–205. https://doi.org/10.1016/j.ijhydene.2021.01.085.

[34] Deb K, Pratap A, Agarwal S, Meyarivan T. A fast and elitist multiobjective genetic algorithm: NSGA-II. IEEE Trans Evol Comput 2002;6(2):182–97. https://doi.org/10.1109/4235.996017.

[35] Seada H, Deb K. U-NSGA-III: A unified evolutionary optimization procedure for single, multiple, and many objectives: Proof-of-principle results. Lect Notes Comput Sci (including Subser Lect Notes Artif Intell Lect Notes Bioinformatics) 2015;9019:34–49. https://doi.org/10.1007/978-3-319-15892-1_3.

[36] Liu Y, Tu Z, Chan SH. Performance enhancement in a H2/O2 PEMFC with dual-ejector recirculation. Int J Hydrogen Energy 2022;47(25):12698–710. https://doi.org/10.1016/j.ijhydene.2022.02.023.

[37] Zhou P, et al. Influence of hydrogen fuel cell temperature safety on bus driving characteristics and stack heating mode. Int J Hydrogen Energy 2022;no. 266. https://doi.org/10.1016/j.ijhydene.2022.07.226.

[38] Li S, Wei X, Yuan H, Ming P, Wang X, Dai H. A galvanostatic charging method for quantitative measurements of hydrogen crossover in fuel cell stack. Int J Hydrogen Energy 2022;no. xxxx. https://doi.org/10.1016/j.ijhydene.2022.09.080.

[39] Ahmadi P, Khoshnevisan A. Dynamic simulation and lifecycle assessment of hydrogen fuel cell electric vehicles considering various hydrogen production methods. Int J Hydrogen Energy 2022;47(62):26758–69. https://doi.org/10.1016/j.ijhydene.2022.06.215.

[40] Deb K, Jain H. An evolutionary many-objective optimization algorithm using reference-point-based nondominated sorting approach, Part I: Solving problems with box constraints. IEEE Trans Evol Comput 2014;18(4):577–601. https://doi.org/10.1109/TEVC.2013.2281535.

[41] Terdich N, Martinez-Botas R. Experimental efficiency characterization of an electrically assisted turbocharger. SAE Tech Pap 2013;6. https://doi.org/10.4271/2013-24-0122.

[42] Liu Y, Madamedon M, Burke R, Werner J. The Experimental Study of the Inner Insulated Turbocharger Turbine. In: ASME 2020 Internal Combustion Engine Division Fall Technical Conference, Nov. 2020. doi: https://doi.org/10.1115/ICEF2020-3042.

[43] Moroz V. Practical Methodologies & Implementations for Turbomachinery Trimming & Scaling. https://www.softinway.com/education/webinars/practical-methodologies-and-implementations-for-turbomachinery-trimming-and-scaling/ (accessed Dec. 14, 2021).